Mémoire

Auteur : Bellon, Kyde
Promoteur(s) : Mahler, Guillaume
Faculté : Faculté des Sciences
Diplôme : Master en sciences spatiales, à finalité approfondie
Année académique : 2024-2025
URI/URL : http://hdl.handle.net/2268.2/23892

Beyond single-plan strong lens modelling: Study of the impact of massive structures along the line-of-sight

Author : Kyde Bellon

Promoter:
Guillaume Mahler

Jury members:
Violeta Gámez Rosas
Dominique Sluse
Gilles Orban de Xivry
Eric Jullo

University of Liège
Faculty of Sciences
Academic Year 2024-2025

Graduation Studies conducted for obtaining the Master's degree in Space Sciences

Abstract

General Theory of Relativity teaches us that a massive object curves the spacetime frame, such that a particle travelling in a straight line would seem to bend around its centre of mass. Gravitational lensing is the result of this effect and is composed of a source emitting photons, one or many deflectors affecting the local spacetime frame and an observer that receives the light that appears bent around the deflectors. In the strong gravitational lensing regime, the observer sees multiple deformed and magnified images of the same source depending on the lens geometry, i.e. the position of the source and the deflector to the line of sight. Understanding and modelling the lens geometry allows us to estimate the total mass and its distribution in the deflector plane. The model can be constructed thanks to parametric methods that explore the parameter space and minimise the differences in position between the images observed and the model predictions. This master's thesis explores the impact of line-of-sight structures between the foreground deflector and the sources at multiple scales. First, we construct single-plane and multi-plane models of the Zig-Zag lens, J1721+8842. Those models have different associations of three image groups that differ in the source and path of the light rays. Their comparison shows different geometries of lenses that retain a similar feature close to the single-plane models for the foreground lens. We compute the total mass of the deflectors and obtain values that differ from the literature. Second, we analyse the overdensity of galaxies between redshifts $z = 1.02$ and $z = 1.09$ of Abell 370 and divide it into three groups. For each of them, the masses are computed using the velocity dispersion, which is obtained based on the redshift of the galaxies. The position of each galaxy in the source plane is computed using an existing model of Abell 370 to find the barycentre of each group. The mass potential of the three groups is then added to the model, generating a displacement of images in the source plane. We show no correlation between the scale of the displacement and the magnification of the images. However, the displacement generated scaled up to 0.6 arcseconds, where the typical root-mean-squared value for position uncertainty of the current best models ranges from 0.2 to 1.0 arcseconds. In both cases, we conclude that line-of-sight structures have a significant impact on the total mass and mass distribution of the foreground structure and lens geometry.

Résumé

La théorie de la relativité générale nous apprend qu'un objet massif courbe le tissu de l'espace-temps de telle sorte qu'une particule voyageant en ligne droite semblera dévier autour de son centre de masse. L'effet de lentille gravitationnelle est le résultat de ce phénomène. Il est composé d'une source émettant des photons, d'un ou plusieurs déflecteurs qui courbent localement l'espace-temps et d'un observateur recevant la lumière de la source dont la trajectoire semble avoir été courbée. Dans le régime fort des effets de lentille gravitationnelle, l'observateur voit des images multiples d'une même source déformées et magnifiées selon la géométrie de la lentille, la position de la source et du déflecteur par rapport à la ligne de visée. Comprendre et modéliser la géométrie de la lentille permet d'estimer la masse totale et sa distribution dans le plan du déflecteur. Le modèle peut être construit grâce à des méthodes paramétriques qui explorent l'espace des paramètres et minimisent la différence en position des images observées avec les prédictions du modèle. Ce mémoire explore l'impact des structures le long de la ligne de visée, placée entre le déflecteur en avant-plan et les sources, et ce à plusieurs échelles. Tout d'abord, nous construisons des modèles à plan unique et multi-plans de la Zig-Zag Lens, J1721+8842. Ces modèles sont composés de différentes associations de 3 groupes d'images qui diffèrent par leur source et le trajet de leurs rayons lumineux. Leur comparaison montre des géométries de lentille différentes qui présentent une caractéristique similaire proche du modèle à plan unique de la lentille en premier plan. Nous calculons la masse totale des deux déflecteurs et obtenons des valeurs différentes de la littérature. Ensuite, nous analysons une surdensité de galaxies situées entre les redshifts $z = 1,02$ et $z = 1,09$ d'Abell 370 et les divisons en trois groupes. Pour chacun d'eux, leurs masses sont calculées via leurs vitesses de dispersion, elles-mêmes obtenues sur base des redshifts des galaxies. La position de chacune des galaxies est calculée grâce à un modèle existant d'Abell 370 pour trouver le barycentre de chaque groupe. Le potentiel massique des trois groupes est ensuite ajouté au modèle, induisant un déplacement des images dans le plan source. Nous montrons qu'il n'y a pas de corrélation entre l'ordre de grandeur du déplacement et la magnification de l'image. Cependant, le déplacement généré peut être aussi grand que 0,6 arcseconde alors que les valeurs typiques d'erreur s'étalent de 0,2 à 1,0 arcseconde pour les meilleurs modèles de lentille. Dans les deux cas, nous pouvons conclure que les structures le long de la ligne de visée ont un impact significatif sur la masse totale et la distribution de masse du déflecteur situé en avant-plan et la géométrie de la lentille.

Acknowledgments

I would like to express my sincere gratitude to my supervisor, Guillaume Mahler, for his guidance, continuous support, and numerous constructive comments, which have greatly enriched this work. His encouragement has been a valuable source of motivation throughout this project. I am also grateful to the Multi-wavelength Extragalactic and Galactic Astrophysics (MEGA) department for their warm welcome and for inviting me to participate in the Extragalactic Journal Club. These stimulating discussions have allowed me to connect different aspects of my coursework and have significantly broadened my scientific horizons.

I would also like to extend my heartfelt thanks to Joyce Dubus and Vincent Mertens, whose constant support throughout the academic year has been invaluable. Their encouragement and help have played an important role in the completion of this work. I wish to thank Anne Bertin and Pauline Gualtieri for their support and kind presence.

Finally, my gratitude goes to Catherine van Dael and Éric Walsdorff, who opened new opportunities for me, helped me gain confidence in myself, and brought a much-needed balance to my daily life.

Taken together, all these experiences and the support I received have made this one of the best years of my studies. This year has allowed me to clearly define the path I want to follow in the future.

Contents

1 Introduction **1**

2 Motivation and Methodology **4**

3 State of the Art **5**
3.1 Lens equations 5
3.2 Lenstool 7
3.3 Multi-plane strong lensing 9
3.3.1 Galaxy-Galaxy case: J1721+8842 10
3.3.2 Cluster-Cluster case: Overdensity of Abell 370 12
3.4 Dynamical mass estimate 13
3.4.1 Median absolute deviation 14
3.4.2 Biweight 14
3.4.3 Gapper 14
3.4.4 Comparison of Biweight and Gapper estimators 15
3.4.5 Relation $\sigma - M$ 17

4 J1721+8842 **18**
4.1 Single-plane models 19
4.2 Multi-plane models 21

5 Abell 370 overdensity between $z = 1.02$ and $z = 1.09$ **27**
5.1 Definition of the groups 27
5.2 Definition of the dPIE potential 28
5.3 Impact of the background groups on the model 30

6 Conclusion and prospectives **31**

A BayesCorner **33**
A.1 Group 1 only 33
A.2 Groups 1 and 3 considered as one group 35
A.3 Groups 1 and 3 considered as different groups 37
A.4 Groups 1 and 3 considered as one group with group 2 39
A.5 Groups 1 and 3 considered as one group with the mass of the foreground lens fixed 41
A.6 Groups 1 and 3 considered as one group with the mass of the background lens fixed 42
A.7 Groups 1 and 3 considered as different groups with the mass of the foreground lens fixed 43
A.8 Groups 1 and 3 considered as different groups with the mass of the background lens fixed 44

Bibliography **45**

1 Introduction

In the early 20th century, Einstein initiated the development of the General Theory of Relativity, which is now the current model of gravitation. General relativity describes gravity as a geometrical property of space and time. A massive object causes the spacetime frame to deform, generating the illusion that a particle travelling straight bends around the centre of mass. In contrast to Newton's theory of gravitation, this effect would also affect massless particles such as photons. A light ray passing by the gravitational potential would follow the geometry and appear deflected. This process is called gravitational lensing, which can be described in three main planes: the observer, the lens, and the source planes. The observer plane is the one in which the telescope is located. The plane at which the effect of the deflector acts by bending spacetime is commonly referred to as the lens plane. The source plane is the one containing the source object, which can be a star, a galaxy, or a cluster of galaxies.
At first, the lens object candidates were thought to be stars deflecting the light of background stars only. For that reason, the first observation of a deflection angle was made during a solar eclipse by Eddington [1], shown in Fig.1, which contributed to the validation of General Relativity.

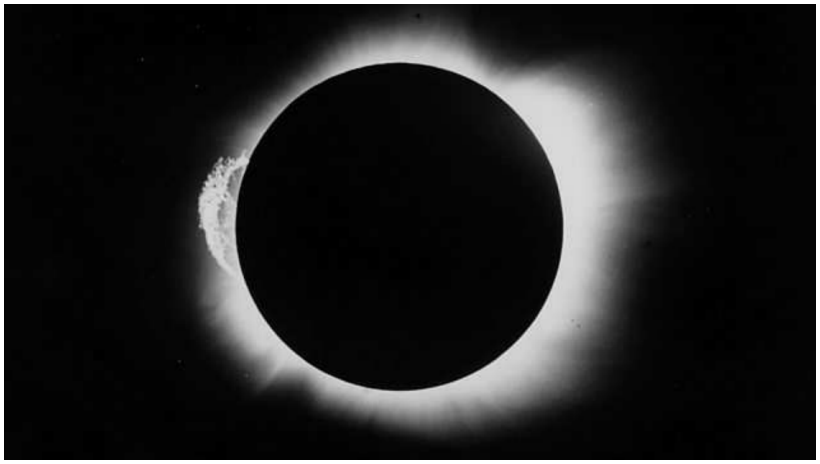

Figure 1: A photograph of the 1919 eclipse, taken at Príncipe (São Tomé and Príncipe), showing a spectacular prominence by Peter Coles [2].

Unfortunately, observing a strong lensing effect of a few arcseconds around stars out of our solar system would be impossible given their mass. However, in 1937, Zwicky proposed that galaxies could also be candidates as a lens, acting as a "natural telescope" for background galaxies. The first observation of a lensed object by a galaxy was realised and confirmed by Walsh*, Carswell, and Weymann in 1979 [1]. As depicted in Fig.2, they observed a twin quasar next to the galaxy Q0957+561.

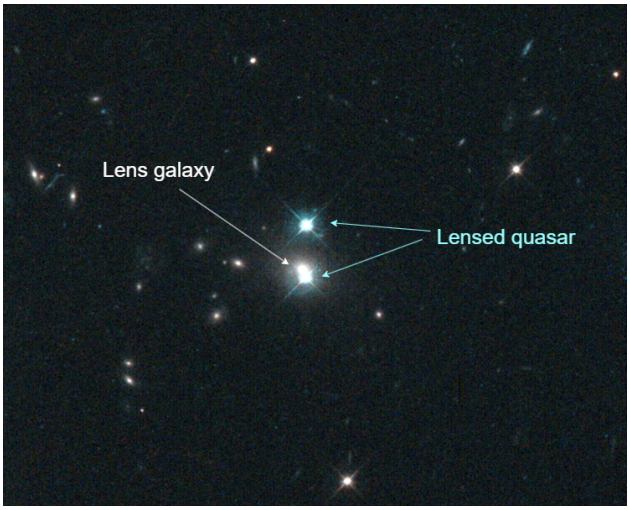

Figure 2: Three colors image of Q0957+561 [3].

In 1988, Soucail et al. presented the ability of clusters to be lens candidates, relating them to arc structures as a consequence of the deformation induced on background galaxies. The first object they present is the giant arc of Abell 370, shown in Fig.3.

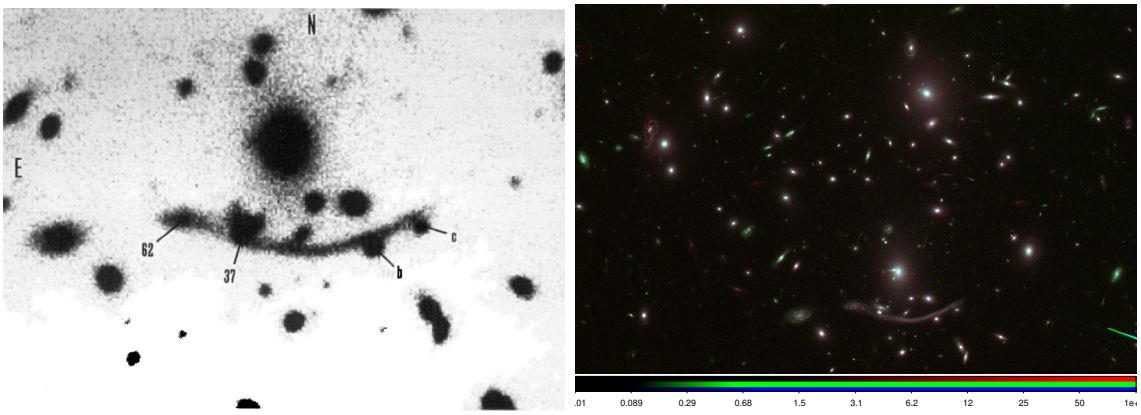

Figure 3: On the left, image of Abell 370 by Soucail et al. [4]. On the right, a three-color image of Abell 370.

More recently, Nayliss et al. determined that the contribution of structures along the line of sight between the source and the lens galaxy cluster on the frequency of strong lenses is non-negligible [5]. Their findings were in line with those of Wambsganss et al. [6] and Puchwein & Hilbert [7]. They estimate an increase in the total strong lensing optical depth and in the lensing cross-section of clusters. This perspective opens the domain to multi-plane gravitational lensing, for which many lens planes are considered between the source and the observer. These line-of-sight structures have to be massive objects, such as a galaxy cluster or a single galaxy. In this case, the galaxy between the source and the lens, having a smaller potential than a cluster, has to be almost perfectly aligned with the line of sight. Otherwise,

the mass potential is too low to cause the spacetime to curve.

While strong lensing is a rare configuration, Kochanek and Apostolakis have explored theoretically the double-plane lensing [8] using two galaxy-like potentials. They estimated a 1% to 10% chance of having two lens galaxies at different redshifts. Later, in 2015, Collett and Bacon [9] show that a double lens can form six images of a background source only if the second lens is multiply imaged by the first. Moreover, the Einstein radius of the second lens must be comparable but not greater than the first. Möller and Blain questioned and evaluated the occurrence of multi-plane lensing by galaxies [10]. According to them, 1 in 20 multiply imaged sources would be a multi-plane lens.

This document explores multi-plane gravitational lensing through two main cases linked to the observations of the Zig-Zag lens, J1721+8842, and the overdensity around a redshift of 1 in Abell 370; see Fig.7 and Fig.3. We quantify the impact of the consideration of the multi-plane lensing compared to the single-plane lensing using model comparison and the measurement of the image position in the source plane. The motivation and method used in this work are presented in the following chapter. The basis of gravitational lensing and multi-plane lensing is then explored, as well as the current understanding of the observations used in this work. The distribution mass model of the gravitational potential in the overdensity of Abell 370 requires estimating the mass based on the velocity dispersion. For this reason, different dynamical mass estimates are presented. In chapter 4, the first focus is the comparison of models of the Zig-Zag lens. Each model has a different set of constraints. Models considering only a single lens plane are compared to multi-plane models, a double plane in this case. The results are also compared to those of Dux et al. [11]. In chapter 5, the overdensity of Abell 370 is subdivided into groups of gravitational potential for which we estimate the mass and compute the barycentre. These results are then used to add new potential to the model of the lens. Their impact is measured thanks to the difference in position of the sources.

2 Motivation and Methodology

This work aims to quantify the impact of the multi-plane lensing effect compared to the model that considered only one lens plane along the line of sight. Considering a galaxy as a source, which is in general a quasar, we identify three multi-plane geometry cases that can be described:

- galaxy-galaxy: a source lensed by a galaxy, then another galaxy;
- cluster-galaxy: a source lensed by a galaxy, then a galaxy cluster;
- cluster-cluster: a source lensed by a cluster, then another cluster.

The differences between them are a less complex mass distribution and a smaller gravitational potential for a galaxy than for a cluster. The first case leads to a double-plane geometry, whereas the cluster can be subdivided into smaller mass potentials, creating a new lens plane for each potential considered.

We first focus on the galaxy-galaxy case, which is represented by the Zig-Zag lens, J1721+8842. At first, in 2018, it was reported as a dual active galactic nucleus (dual-AGN) candidate by Lemon et al. [12] and confirmed through spectroscopy as a double lens by Dux et al. [11]. The simplicity of this double lens would help to understand the basis of multi-plane lensing. With one of the two lens planes being lensed, the object lying there becomes both a source and a deflector. This double role in the lens geometry might be difficult to handle and is tested in chapter 4.

The second focus of this work is the overdensity of the galaxy between redshifts $z = 1.02$ and $z = 1.09$ in Abell 370, identified thanks to spectroscopy by Lagattuta et al. [13]. This covers the cluster-cluster case. The overdensity is divided into groups of galaxies based on their dispersion velocity computed from their redshift. The mass barycentre of each group is then computed to place the dark matter potential of the object. The distribution of the latter is discussed in chapter 5. The difference in the position of the images obtained from different models is finally compared to understand the influence of each group on the deviation of the light along the line of sight.

In the first case, the parametric software Lenstool is used to compute the model of the lenses. This one is based on a Bayesian approach of a Monte-Carlo Markov Chain. Models are obtained by finding the closest prior PDF to the posterior one. A pseudo-isothermal elliptical mass distribution is used to represent the mass distribution of the galaxy and cluster.
In the second case, the same software is first used with an existing model of Abell 370 to obtain the position of each galaxy for each group in the source plane to compute its barycentre. The position of the image, accounting for the structures along the line of sight, is computed using this same model in addition to the mass potential of each group.

3 State of the Art

Three different configurations of the lensing effect can be described: strong lensing, weak lensing, and microlensing. In any case, the light rays follow a geodesic and appear as bent by a mass potential. The strong lensing case describes the case where the wave fronts are sufficiently deflected to overlap enough such that, reaching the observer, multiple images can be resolved, as shown in Fig.4. It leads to several images of the source, magnified or demagnified. The weak lensing corresponds to the case where the alignment along the line of sight does not allow the formation of multiple images but only the convergence and shear induced by the lens. The microlensing corresponds to the unresolved case where the images are too close to be resolved by the current telescopes.

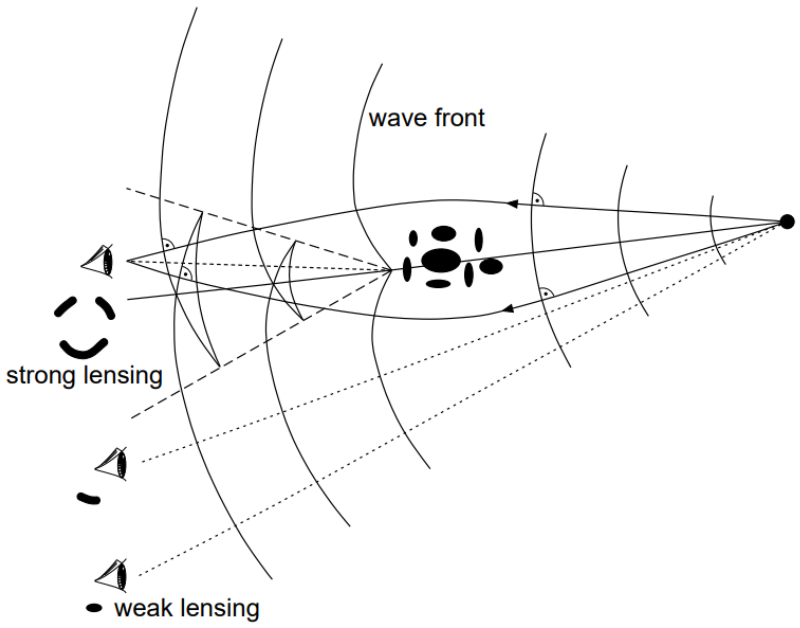

Figure 4: Wave fronts and light rays in the presence of a cluster perturbation by N. Straumann [14].

This work focuses on strong lensing, which is nowadays used to probe mass potentials and dark matter distribution in galaxies and clusters. Lensing does not rely on kinematic effects and makes no assumptions about the dynamic state of the lens. Another advantage of lensing is its achromatic property, producing the same signal at all frequencies and making information combination easy from multi-wavelength data sets [15].

3.1 Lens equations

The lens equation relates the position of a source to its image. It can be retrieved from a geometrical construction. In this thesis, a few assumptions are considered. The first is

the thin lens approximation: the deflecting mass is considered to lie on a single plane, the lens plane. The distribution of the lens mass along the line of sight is considered negligible regarding the distance to the observer and the source.
Following this, the gravitational lensing is composed of 3 planes: the observer, the lens, and the source plane, as shown in Fig.5. From these planes and the line of sight, the following distances and angles can be defined:

- D_L the distance between the observer and the plane of the lens;
- D_S the distance between the observer and the source;
- D_{LS} the distance between the plane of the lens and the plane of the source;
- ξ the distance between the image and the centre of mass of the lens, both in the lens plane;
- a the distance between the image and its source, both in the plane of this one;
- b the distance between the line of sight of the observer and the source, both in the plane of this one;
- c the distance between the line of sight of the observer and the image, both in the plane of the source, which is equivalent to the sum of a and b;
- α the deflexion angle between the source and its image;
- β the angle between the optical centre and the real position of the source;
- θ the angle between the optical centre and the image of the source.

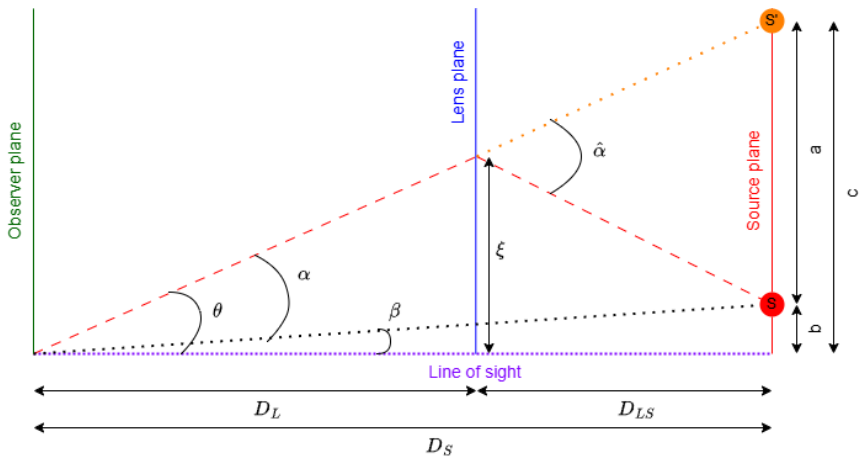

Figure 5: Scheme of single-plane gravitational lensing effect. The centre of mass of the lens is placed at the intersection of the lens plane and the line of sight. S is the source, and the red dashed line is a light ray coming from it. The orange dotted one corresponds to the projection of the image from the lens plane onto the source plane.

Using the assumption of a large distance between the three planes, combined with the geometry of the problem, leads to the small-angle approximation. Allowing us to write the relations,

$$a \approx \alpha\, D_{LS} \qquad b \approx \beta\, D_S \qquad c \approx \theta\, D_S. \tag{1}$$

Such that we can assume a flat Universe. A relation between the distances can be written,

$$D_s = D_L + D_{LS}. \tag{2}$$

The deflection angle for any lens is expressed as

$$\alpha(\xi) = \frac{4\,G}{c^2} \iint \frac{\Sigma(\xi')(\xi - \xi')}{|\xi - \xi'|^2} d^2\xi. \tag{3}$$

By application of the thin lens approximation, $a + b = c$, leading to

$$\theta = \beta + \hat{\alpha}(\theta)\, \frac{D_{LS}}{D_S} \tag{4}$$

From which we obtain the lens equation

$$\beta = \theta - \alpha(\theta) \qquad \text{where} \qquad \alpha(\theta) = \hat{\alpha}(\theta)\, \frac{D_{LS}}{D_S} \tag{5}$$

The formation of multiple images, and thus the separation between strong and weak lensing, occurs when the mean surface density Σ is greater than the critical density Σ_{cr}, respectively expressed as

$$\Sigma = \frac{M}{\pi\xi^2} \quad \text{and} \quad \Sigma_{cr} = \frac{c^2}{4\pi G} \frac{D_{LS}}{D_L\, D_S}. \tag{6}$$

These equations describe the way a source will be affected by the lens. To find the source position and probe the mass from the detection of multiple images, these equations must be inverted. An optimisation implementation is required to fit the best lens model to the constraints, primarily the position of the images.

Where most studies assumed a specific cosmology (generally $\Omega_M = 0.3$ and $H_0 = 70\,km/s$), several others claim that the parameter uncertainties could be non-negligible compared to those brought by the lensing model. Bayliss et al. [16] have shown a significant magnification uncertainty correlated to the variation of cosmological parameters. This last study does not account for the effect of structures along the line of sight.

3.2 Lenstool

To model strong lenses, the public software package LENSTOOL is used to invert the lens equation with parametric methods by exploring the parameter space. Gravitational lensing

transforms the source position in the source plane, β, to the image position in the image plane, θ, and is expressed as [17]

$$\beta = \theta - \nabla\psi(\theta) \tag{7}$$

where $\psi(\theta)$ is the lens potential at the image position, expressed as

$$\psi(\theta) = \frac{2}{c^2}\frac{D_{LS}}{D_S}\,\phi(\theta) \tag{8}$$

with $\phi(\theta)$ the projected Newtonian potential, defined by the mass distribution of the lens. This leads to a direct mass constraint when the distance to the lens and source is known. To fit the lens model, a Bayesian Markov Chain Monte-Carlo (MCMC) is used to explore the parameter space and provide model comparison. This approach defines the prior PDF as the probability of getting the parameters given the model, $P(\theta|M)$, the posterior PDF as the one of getting the parameters given the model and the observed data, $P(\theta|D, M)$, the likelihood as the one of getting the observed data given the parameters and the model, $P(D|\theta, M)$, and the evidence, $P(D|M)$. Relating all these probabilities by the Bayes theorem,

$$P(\theta|D, M) = \frac{P(D|\theta, M)\,P(\theta|M)}{P(D|M)} \tag{9}$$

A burn-in phase is implemented to explore most of this parameter space and avoid local minima in the likelihood functions. This is obtained using the unnormalised posterior PDF, which is the product of the likelihood and the prior. The model comparison requires the normalisation of the posterior, which is the evidence. The model with the prior PDF closest to the posterior PDF is considered the best solution. In other words, the scatter between the observed and predicted lensing evidence is minimised [18].

The parameters used by the solver are the position (x_c, y_c), the projected ellipticity ε_Σ, the position angle PA, and other specific parameters related to the model chosen. In this paper, the dual Pseudo Isothermal Elliptical model (dPIE), a.k.a. the Pseudo-Isothermal Elliptical Mass Distribution model (PIEMD), is chosen to represent the mass of galaxies and clusters, offering flexibility to add a cored profile. It is often used in literature, for example, in the study of Mahler et al. [19], Lagattuta et al. [13], and Sharon et al. [18]. This model defines three regions of density following a different profile in these regions, as shown in Fig.6. The first region, between the core and r_{core}, is constant with the radius. The second one, between r_{core} and r_{cut}, decreases proportionally to r^{-2}. The last region, from r_{cut}, has a faster decrease proportional to r^{-4} [20].

Such that the 3D density distribution is expressed as

$$\rho = \frac{\rho_0}{(1 + \tilde{R}^2/r_{core}^2)(1 + \tilde{R}^2/r_{cut}^2)} \quad \text{with} \quad \rho_0 = \frac{\sigma_\infty^2}{2\,\pi\,G\,r_{core}^2} \tag{10}$$

and the ellipticity is obtained based on projected ellipticity ε_Σ,

$$\varepsilon_\phi = \frac{1 - \sqrt{1 - \varepsilon_\Sigma^2}}{\varepsilon_\Sigma}. \tag{11}$$

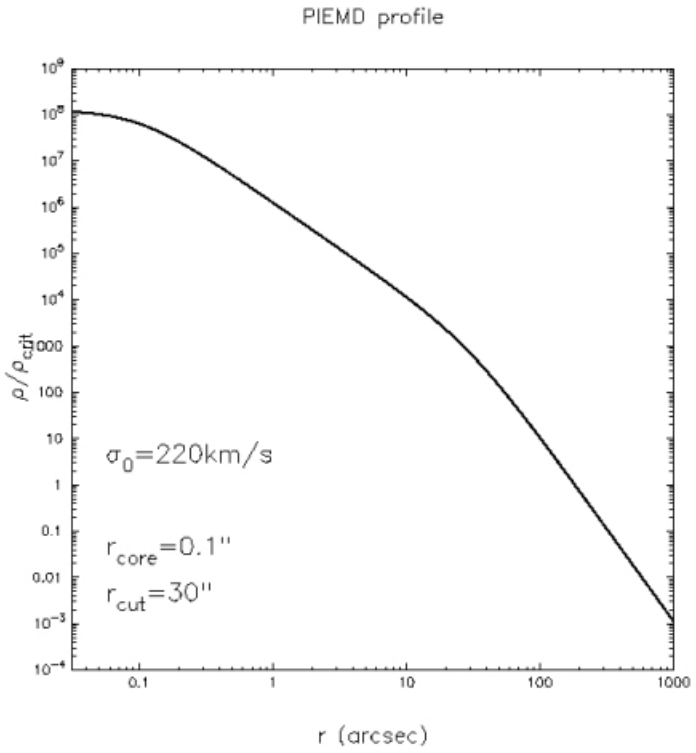

Figure 6: Example of dPIE profile by Limousin [21].

In LENSTOOL, it results in an expression for the fiducial velocity dispersion

$$\sigma_{dPIE}^2 = \frac{4}{3} G \pi \rho_0 \frac{r_{core}^2 r_{cut}^3}{(r_{cut} - r_{core})(r_{cut} + r_{core})^2} \tag{12}$$

which leads to a constraint on the mass of the object based on σ_{dPIE}, r_{cut} and r_{core}.

3.3 Multi-plane strong lensing

Among the rare cases of strong lensing, some may involve multi-plane strong lensing. This occurs when many deflectors are more or less aligned along the line of sight. The light rays would first be lensed, creating one or multiple images that are lensed by a foreground deflector.

The light rays follow the geodesic equation, specialised to a perturbed Robertson–Walker metric. A continuous formalism in arbitrary spacetimes can be used to describe the propagation of light between the main lens planes, resulting in distance matrices between lens planes as solutions of the equation (referenced as the optical tidal equation in the Schneider paper [22]).

In this work, we focus on two types of deflectors: a galaxy or a cluster of galaxies. Two cases are studied and represented by the Zig-Zag lens, J1721+8842, and the overdensity between $z = 1.02$ and $z = 1.09$ in Abell 370. The last one is not covered in this paper.

3.3.1 Galaxy-Galaxy case: J1721+8842

In 2018, J1721+8842 was reported as a quadruply imaged source at redshift $z = 2.38$ among others using *Gaia* observation by Lemon et al. [23]. Which has been interpreted as a lensed dual active galactic nucleus (dual-AGN) at redshift $z = 2.38$ separated by 0.7" (6 kpc) by Lemon et al. [12]. This lens is shown in Fig.7 and has the coordinates: RA 260.45419°, DEC 88.70621°. The Einstein radius has been estimated to $1.99^{+0.01}_{-0.01}$ arcseconds and the total source magnification to 27^{+6}_{-4}. Thanks to the Pan-STARRS images, they also detect the arc present in this lens without the ability to say if it belongs to the lens quasar or another source.

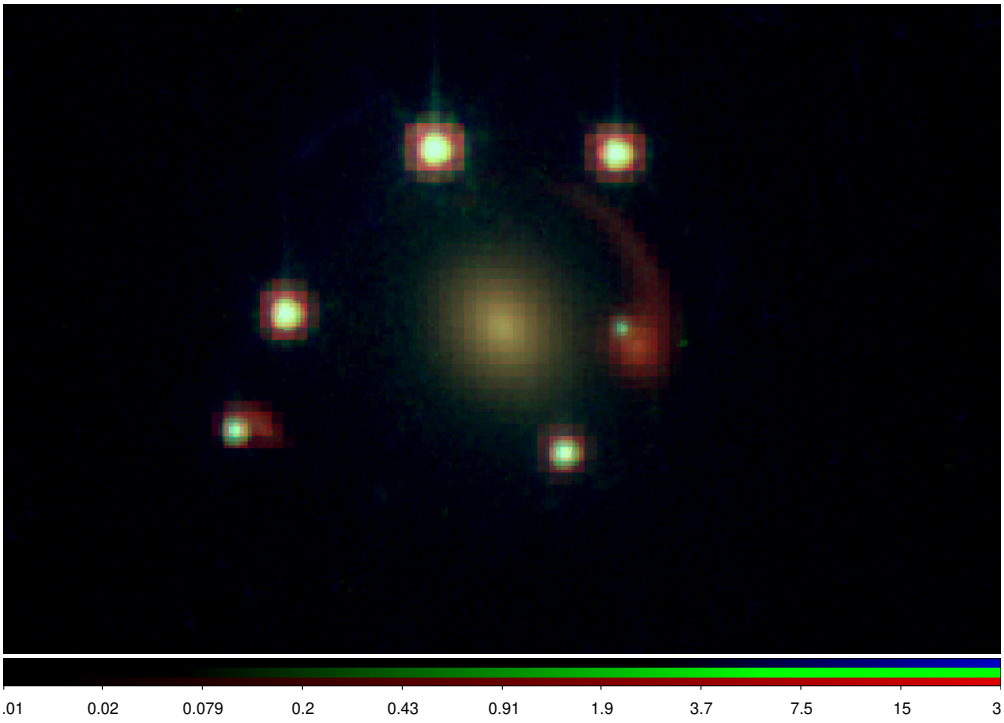

Figure 7: Three colors image of the Zig-Zag lens, J1721+8842.

In 2024, Dux et al. confirmed that the two quasars are the same, with different optical paths. Some images are the result of the gravitational lensing by the foreground galaxy. The ones lying near the arcs are formed from the images resulting from the gravitational lensing effect around a galaxy, at the origin of the arc, lying between the quasar and the foreground galaxy [11].

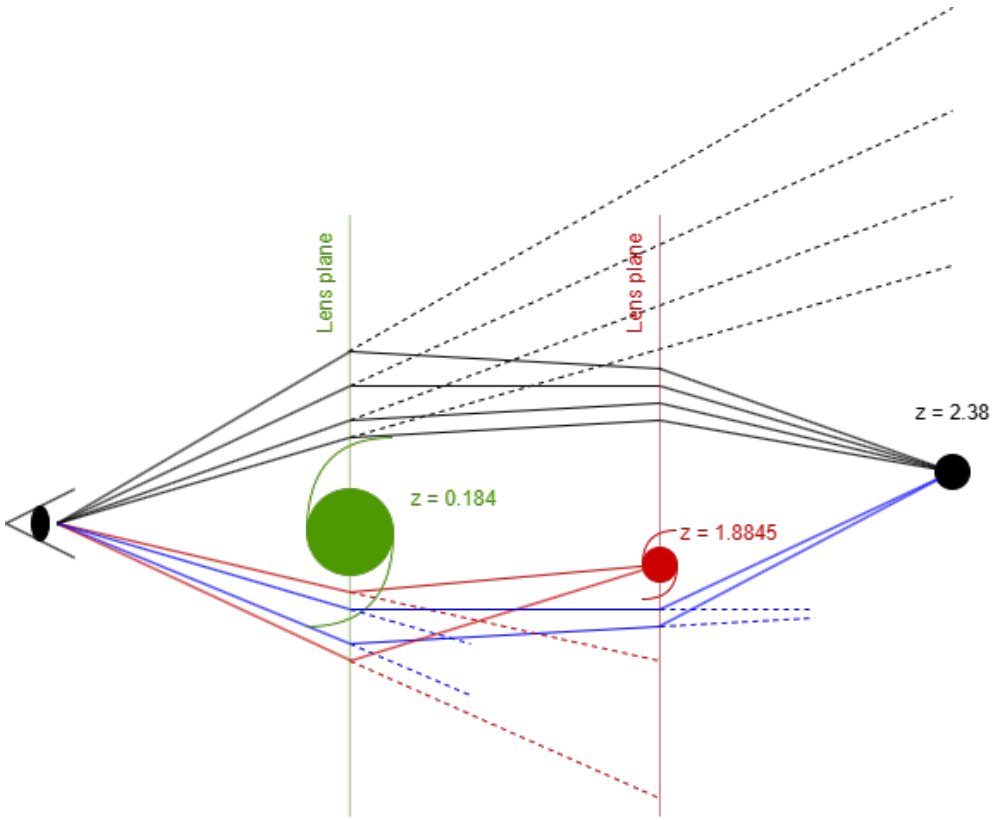

Figure 8: Scheme of the Zig-Zag lens system. The red lines represent the light rays coming from the galaxy which is both a deflector and a source. The blue ones represent the light rays coming from the background quasar that are lensed twice.

With this consideration, they re-evaluated the redshift of the quasar to be $z = 2.382 \pm 0.002$, which is in agreement with the previous studies. Their evidence are:

- the identical light curves that are shifted by about 35 days;
- the redshift of the lensed arc, $z_2 = 1.8845$, lying between the foreground galaxy, $z_1 = 0.184$, and the quasar, $z_{source} = 2.38$;
- the lens model that uses the multi-plan configuration can reproduce the lens with a root-mean-squared error (rms) of 0".03, which is really small compared to the rms obtained for lens models.

From their lens model, they find the Einstein radius of this foreground lens to be $\theta_{E,2} = 0.359 \pm 0.014$", and a total enclosed mass of $M_2 = (2.31 \pm 0.19) \cdot 10^{11} M_{\odot}$. The same quantities can be found for the galaxy lensed, whose Einstein radius is $\theta_{E,1} = 1.744 \pm 0.013$", leading to a total enclosed mass of $M_1 = (2.74 \pm 0.04) \cdot 10^{11} M_{\odot}$.

3.3.2 Cluster-Cluster case: Overdensity of Abell 370

With the release of the Frontier Fields program images [24], several studies have shown that substructure populations lie in the clusters observed, among which is Abell 370. Thanks to the Multi-Unit Spectroscopic Explorer (MUSE), the redshift of the galaxies present in the cluster can be measured. Line-of-sight substructures can be found by analysis of their distribution by redshift (e.g. Lagattuta et al. [13]). A scheme of the influence of substructures on the line of sight is shown in Fig.9.

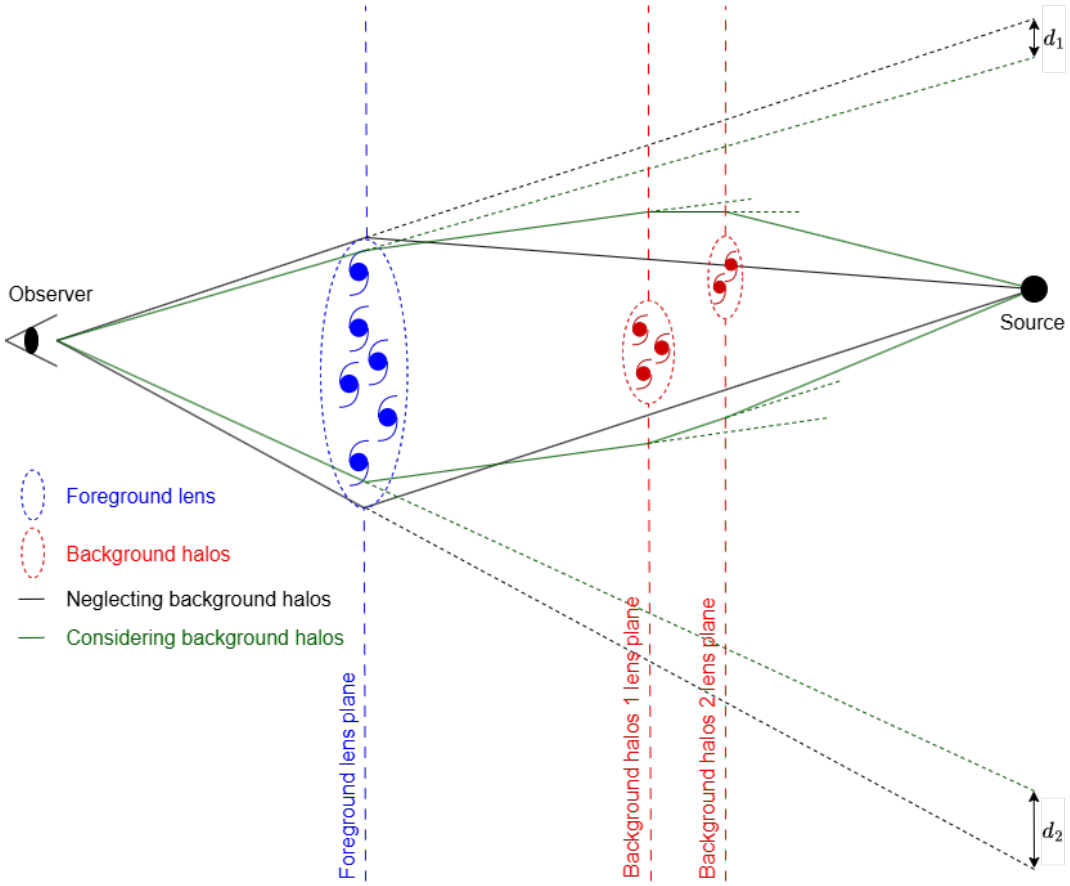

Figure 9: Scheme of Abell 370 overdensity of background halos inducing multi-plane strong lensing. d_1 and d_2 are the distances between the images in the source plane with and without considering the influence of the background halos.

In many lens models, it is a common practice to artificially add an external shear field (e.g. Mahler et al. [19], and Niemiec et al. [25]). This covers tidal perturbations due to external structures (along the line-of-sight, or outside of the modelled field-of-view) and corrects most of the approximations made in the potential or lens model. The overdensity of galaxies at $z \approx 1$ in Abell 370 might be at the origin of the high mass external shear computed by Lagattuta et al. in 2019 [26]. Assuming the median redshift $z = 1.054$, this group has a physical diameter of 534 kpc centred on coordinate $\alpha = 39.9709852$, $\delta = -1.5751906$ [13].

3.4 Dynamical mass estimate

To build the mass potential, we use a dPIE (a.k.a. PIEMD) model, which needs as input the fiducial velocity dispersion that can be obtained by fixing the r_{cut}, r_{core} and the mass. r_{core} will be fixed to zero, the r_{cut} to R_{200} and the mass to M_{200}.
The subscript 200 corresponds to the overdensity constant Δ_c. By convention, the value of Δ_c is set to 200, 500, or 1000. For example, M_{200} means 200 times the critical mass of the Universe, considering the average mass of the Universe at the time at which the cluster is lying.
Those values are obtained by application of the Virial theorem to a sphere. The Virial theorem links the average kinetic energy $\langle T \rangle$ to the average potential energy $\langle U \rangle$,

$$\langle T \rangle = -\frac{1}{2}\langle U \rangle. \tag{13}$$

A sphere in which the Virial theorem is verified has a radius r_{vir}, the Virial radius, and a halo's mean density defined such that the density contained in this radius is equivalent to the critical density of the Universe ρ_c multiplied by the critical overdensity constant Δ_c,

$$\rho(< r_c) = \Delta_c \, \rho_c(t) = \Delta_c \frac{3H^2(t)}{8\pi G} \tag{14}$$

as the critical density is defined as

$$\rho_c(t) = \frac{3\,H(t)^2}{8\,\pi\,G}. \tag{15}$$

The Virial mass can be defined as

$$M_c = \frac{4}{3}\pi\, r_c^3\, \rho(< r_c) = \frac{\Delta_c\, H^2(t)}{2\,G}\, r_c^3. \tag{16}$$

To obtain the value of M_{200}, we replace Δ_c by 200,

$$M_{200} = \frac{4}{3}\pi\, R_{200}^3\, \rho(< R_{200}) = \frac{200\, H^2(t)}{2\,G}\, R_{200}^3. \tag{17}$$

The mass M of a galaxy cluster can be estimated based on the dynamics of this cluster. To do so, it is first required to compute the dispersion velocity of the group, σ, from the redshift of the galaxies, z. In this work, the definition of a group is based on a maximum threshold on the velocity within the group. The computation of this velocity follows the expression

$$\Delta v = c\, \frac{|z_g - z|}{1 + \frac{z_g + z}{2}} \tag{18}$$

A Gaussian distribution of radial velocities is assumed. To minimise the variance of the estimator, be resistant in the presence of outliers and robust for a broad range of non-Gaussian populations, different estimators proposed by Beers et al. [27] are used.
In the following description of the estimators, a sample $x_i = \Delta v_i$, with $i = 1, ..., n$, sorted in ascending order, is considered. The sample median is defined as

$$M = \begin{cases} x_{k+1} & \text{for } n = 2k+1, \\ \frac{1}{2}(x_k + x_{k+1}) & \text{for } n = 2k. \end{cases} \tag{19}$$

3.4.1 Median absolute deviation

From the median M of the sample, the median absolute deviation or MAD is defined as

$$\text{MAD} = median(|x_i - M|). \tag{20}$$

This estimator is tolerant to some asymmetry in the sample, using the median rather than the average. The standard deviation S_{MAD} is found normalising for a standard normal population, $\mathcal{N}(0, 1)$,

$$S_{\text{MAD}} = \frac{\text{MAD}}{0.6745}. \tag{21}$$

It has been shown that these estimators give rather good results for a sample as small as $n = 20$.

3.4.2 Biweight

The biweight estimator aims to do better than the MAD but is more complex to compute, which can be done in one step or with an iterative process. The one-step method has been used in this thesis.
The scale estimator S_{BI} is based on the median M, the MAD and the tuning constant $c = 9.0$, defining

$$u_i = \frac{x_i - M}{c\,\text{MAD}} \tag{22}$$

leads to

$$S_{BI} = n^{1/2} \frac{[\sum_{|u_i|<1}(x_i - M)^2(1 - u_i^2)^4]^{1/2}}{|\sum_{|u_i|<1}(1 - u_i^2)(1 - 5u_i^2)|}. \tag{23}$$

Giving good results for samples as small as $n = 10$.

3.4.3 Gapper

This estimator is based on the gaps between the order statistics, defined as

$$g_i = x_{i+1} - x_i \quad \text{for } i = 1, ..., n - 1, \tag{24}$$

and the set of Gaussian weights

$$w_i = i(n - i). \tag{25}$$

Leading to the following expression for the gapper scale estimator,

$$S_G = \frac{\sqrt{\pi}}{n(n-1)} \sum_{i=1}^{n-1} w_i\, g_i. \tag{26}$$

Resulting in a robust estimator even for samples as small as $n = 10$.

3.4.4 Comparison of Biweight and Gapper estimators

These estimators evaluate the same quantity of dispersion velocity and must therefore converge to the same values for an increasing number of galaxies in the batch. The comparison of the methods would ensure the correct implementation of the estimators.
This is tested by creating a batch of a given number of galaxies with a redshift following a normal distribution. The velocity dispersion of this batch is then computed using both estimators. The result comparison is shown in Fig.10.

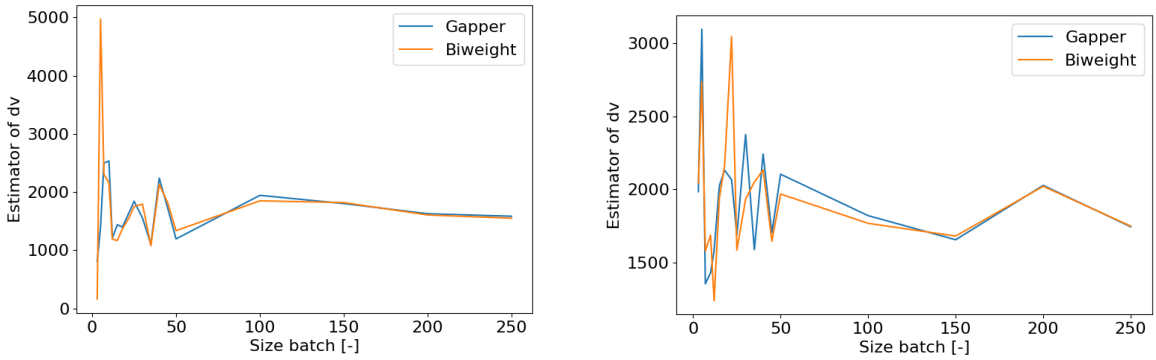

Figure 10: Two convergence tests for the gapper and biweight estimators.

In these figures, we can see that both methods give similar results, especially when the number of galaxies in the batch is high. Whereas this is verified for most of the batch tested, some problems arise for certain samples. This is shown in Fig.11, where the vertical axis is the relative difference between the two estimators, which is expressed as

$$\text{Relative difference} = \frac{\text{Gapper} - \text{Biweight}}{\text{Biweight}}. \tag{27}$$

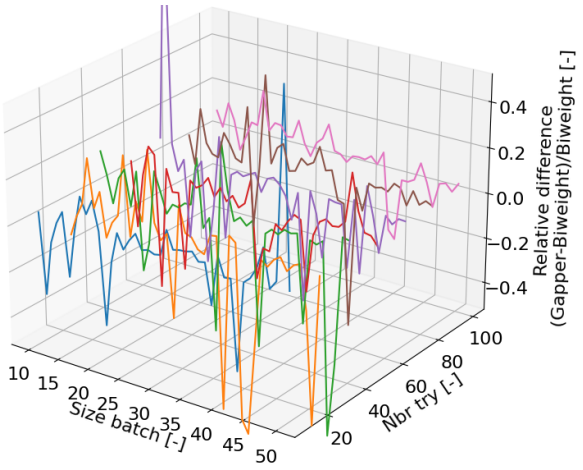

Figure 11: Repetition of the convergence test for the gapper and biweight estimators. For visibility, only a few tests are plotted here.

The problems are due to the creation of a batch that is too widely distributed, resulting in a negative velocity dispersion obtained with the biweight estimator.

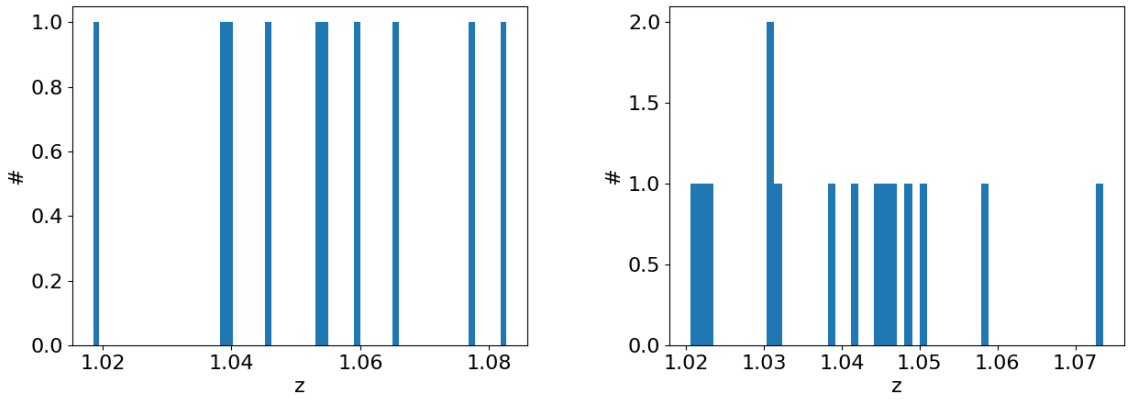

Figure 12: Two examples of a distribution created following a normal distribution that leads to an error in the biweight estimator.

To overcome this problem, we simply remove the cases leading to a negative velocity dispersion and repeat the test until we reach 1000 repetitions. The results are displayed in Fig.13.

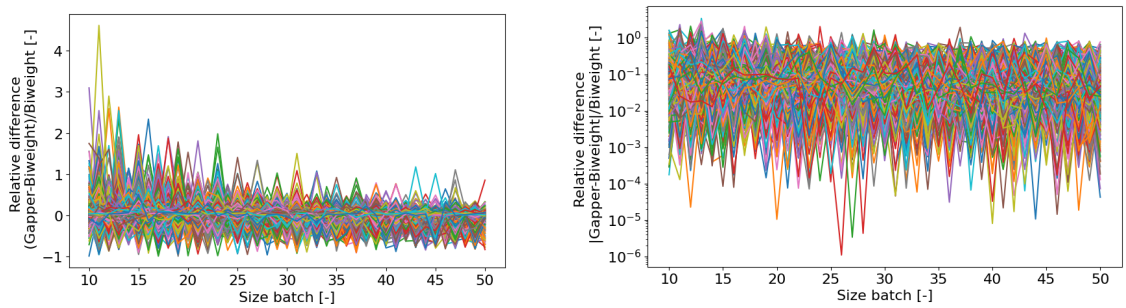

Figure 13: 1000 repetitions of the convergence test for the gapper and biweight estimators, removing the problematic cases. On the left, the vertical axis is in a linear scale. On the right, the absolute value of the relative difference is taken and plotted on a logarithmic scale.

From this last test, we see that the relative difference decreases with the increase in the size of the batch. However, some widely distributed batches do not lead to a negative value, but with one close to zero are still present in the test. They lead to the highest difference values. For a batch size equal to 50 galaxies, we have a minimum relative difference of the order of 10^{-4} and a maximum of 0.8.

Another solution to avoid the negative velocity dispersion might be to use a bootstrap method. That was not implemented here, as the convergence between the methods is already verified when the problematic cases are removed.

3.4.5 Relation $\sigma - M$

The final step to characterise the mass of a galaxy cluster from the velocity dispersion is to use an empirical $\sigma - M$ relation. Today, many relations have been proposed, with some based on cosmological simulations such as the one proposed by Ferragamo et al. [28], which is a power law with a dependence on z.

$$\frac{\sigma_{200}}{km/s} = A\left(\frac{h(z)\,M_{200}}{10^{15}M_{\odot}}\right)^{\alpha+\beta\,z} \tag{28}$$

where A, α and β are parameters calibrated using The Three Hundred dataset. Their values depend on the hydrodynamical simulation codes *Gadget-X* and *GIZMO-SIMBA* and are listed in Table 1.

	A	α	β
Gadget-X	1216.2 ± 0.6	0.358 ± 0.002	0.027 ± 0.003
GIZMO-SIMBA	1198.8 ± 0.7	0.341 ± 0.002	0.026 ± 0.002

Table 1: Best fit parameter of equation 28 for sub-halos by Ferragamo et al. [28].

Inverting this relation allows us to obtain the mass expressed in $10^{15}M_{\odot}$.

$$\frac{h(z)\,M_{200}}{10^{15}M_{\odot}} = \left(\frac{1}{A}\frac{\sigma_{200}}{km/s}\right)^{\frac{1}{\alpha+\beta\,z}} \tag{29}$$

This relation will be used further in this work to estimate the mass of the sub-halos lying behind Abell 370.

4 J1721+8842

The goal of this chapter is to compare different models of a galaxy-galaxy double-plane lens. The Zig-Zag lens, J1721+8842, has been reported and presented as a dual-AGN by Lemon et al. [23] [12]. Later, Dux et al. confirmed the double-plane lens using spectroscopy to compute the redshift. This lens configuration leads to the creation of six images of the background quasar and two images of the galaxy lying between the quasar and the foreground galaxy [11].

The lensed images are distinguished into 3 groups :

- group 1: 4 images of a quasar lensed by J1721+8842;
- group 2: 2 images of a galaxy lensed by J1721+8842;
- group 3: 2 images of a quasar, close to group 2.

This last group is claimed to be the image of the same quasar as group 1, according to Dux et al. [11], unlike previous studies. Meaning that the group 3 images are the result of lensing by the galaxy of group 2, then by J1721+8842. Group 3 would have the same source as group 1, but different optical paths.

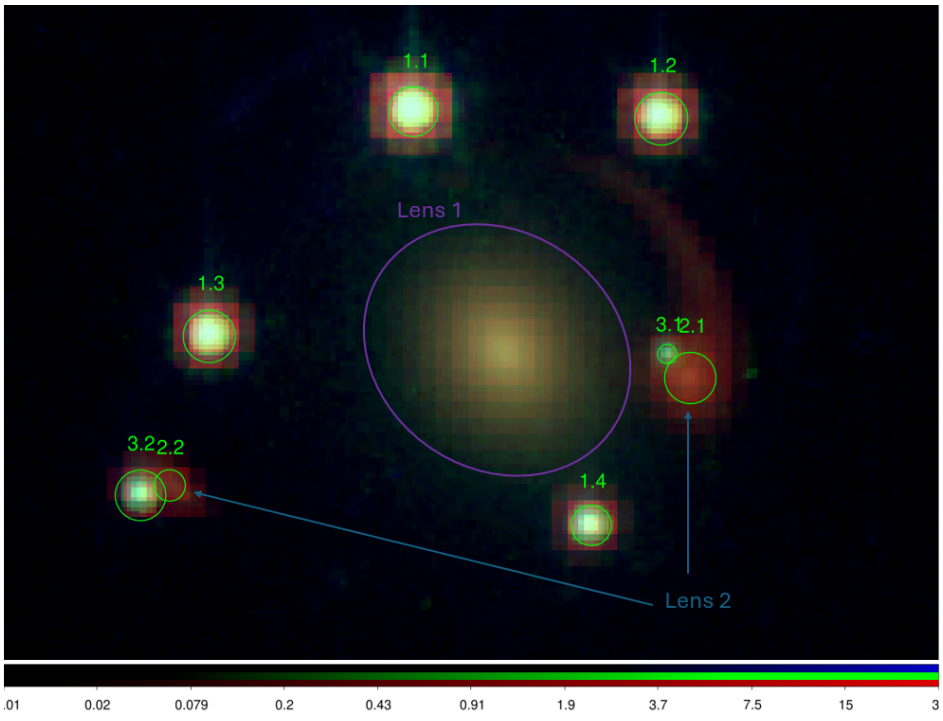

Figure 14: Group of images definition and lenses for J1721+8842. The foreground lens is marked as Lens 1 and the background one as Lens 2.

4.1 Single-plane models

Four models were constructed using different combinations of groups, with group 1, allowing for the analysis of the impact of groups 2 and 3 on the model. Here, the models are presented before the comparison.

The first model, shown in Fig.15a, uses only group 1 to constrain the model of the lens, which suggests that this one should have the greatest uncertainty. However, this model gives a good characterisation of the lens, retrieving all the images of the group. The critical and caustic line positions are coherent with the position and the same as the lens. The second model, shown in Fig.15b, uses groups 1 and 2. Small variations of the model can already be seen compared with the previous model. The position of some images of group 1 seems to have been slightly shifted toward the lens. The third model, shown in Fig.15c, utilises groups 1 and 3. The model is not expected to superimpose images of groups 1 and 3, which does not mean that these are different objects, but highlights the different optical paths of the groups, as explained previously. In this model, the 3.1 image is small compared to the others. The centre of images 3.1 and 3.2 seems more shifted than the other, only due to the size of the region defining 3.1. The last model, shown in Fig.15d, combines the three groups. This model gives a better fit of group 3 images, while images of group 1 at 1.3 are shifted towards the centre.

The comparison of the χ^2, the root-mean-squared on the images rms_i, the likelihood in log scale and mass of the foreground lens M_1 of the different models is shown in Table 2. The mass of the lens is computed from the mass distribution maps at the redshift of the lens. The region from which we obtain the mass is centred on the lens centre of mass and expands to the farthest image.

Group	1	1 and 2	1 and 3	1, 2 and 3
χ^2_{tot}	0.13	0.95	0.59	0.78
rms_i	0.04	0.08	0.06	0.06
log(Likelihood)	5.46	7.81	7.99	10.66
$M_1[10^{12} M_\odot]$	0.6410	0.6088	0.6218	0.6144

Table 2: Comparison of statistical tools output and mass of the foreground lens between different models. Only one lens plane is considered.

We can note that the likelihood increases with the amount of information given to build the model. All these models propose a mass for the foreground lens greater than the mass computed by Dux et al. [11], which is equal to $M_1 = (2.74 \pm 0.04) \cdot 10^{11} M_\odot$. An additional model has been constructed to test if the model recovers the redshift measured by spectroscopy for group 3. This model is shown in Fig.16. It finds the value $z = 2.19 \pm 0.2$ and $M_1 = (6.67 \pm 0.6) \cdot 10^{11} M_\odot$, which is in the same order as the reference. The error in the value could not be measured as only one test has been constructed. By default, we estimated the error to be 10% of the value.

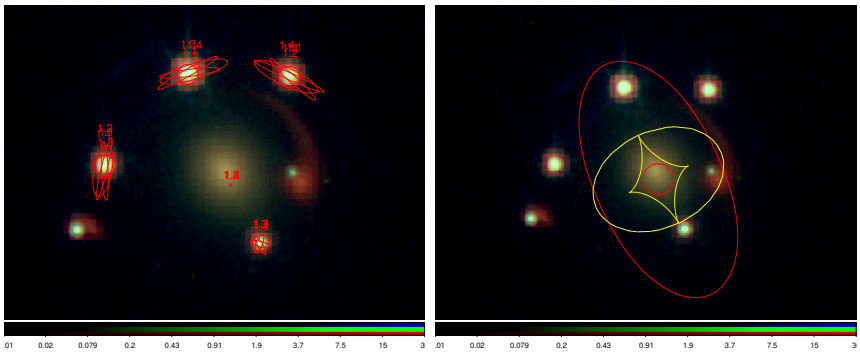

(a) Model of J1721+8842 using group 1.

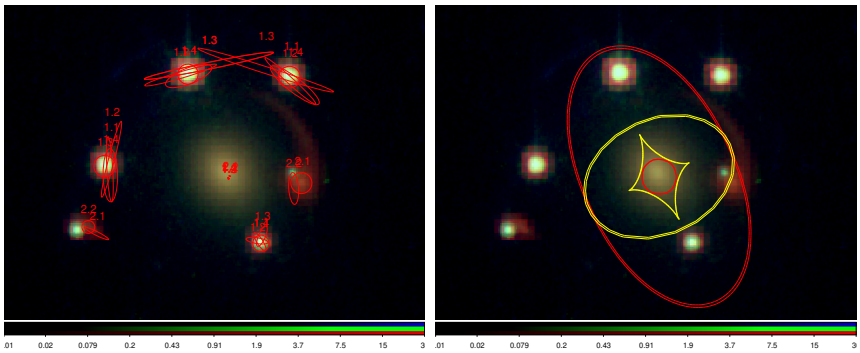

(b) Model of J1721+8842 using group 1 and 2.

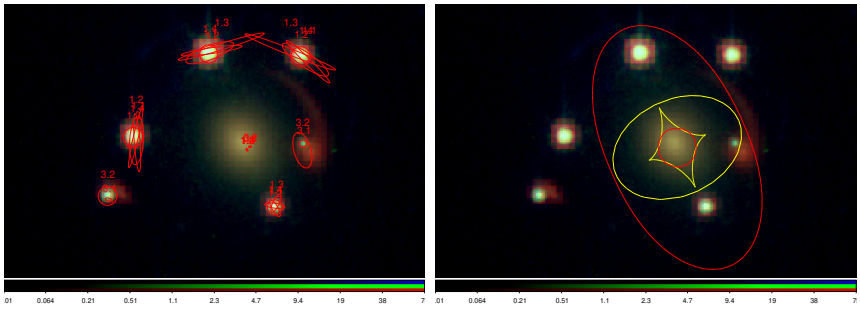

(c) Model of J1721+8842 using group 1 and 3.

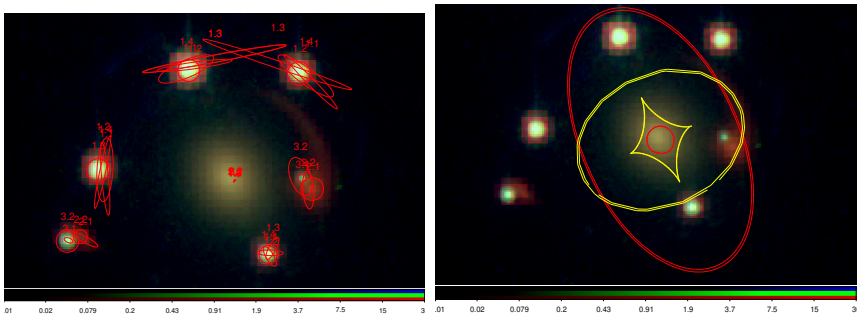

(d) Model of J1721+8842 using groups 1, 2, and 3

Figure 15: Models of J1721+8842 considering only one lens plane. On the left, the images of the quasar lensed by the main galaxy are shown in red. We see that the centre of the region is well placed over the one observed. On the right, the critical and caustics lines, respectively in red and yellow, are drawn in the lens and source plane z = 2.38.

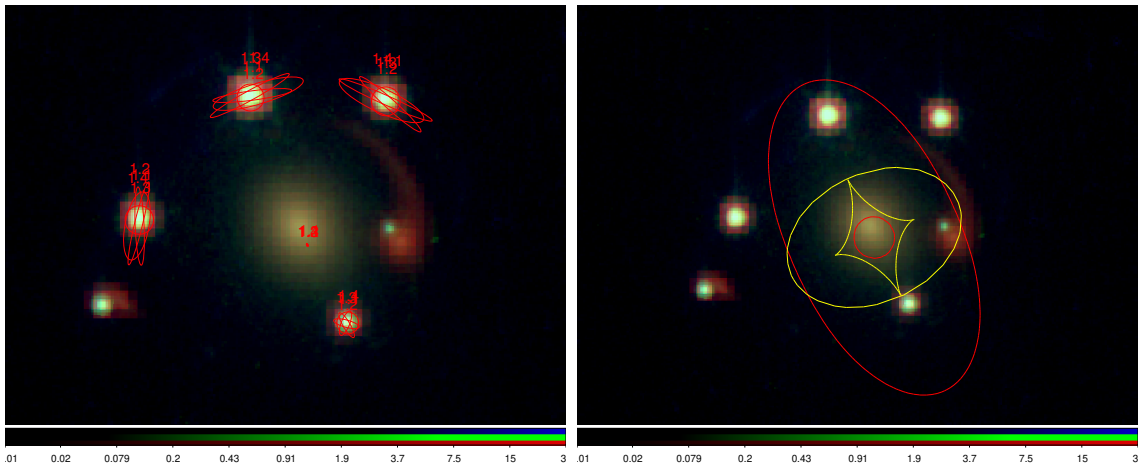

Figure 16: Model of J1721+8842 using groups 1, 2 and 3 without the information on the redshift for group 3.

4.2 Multi-plane models

Now, we add a second potential in the lens model and use LENSTOOL to optimise the multi-plane configuration. Four models are built based on different combinations of the groups:

- Group 1 only;
- Groups 1 and 3 are considered in the same system;
- Groups 1 and 3 are considered in a different system;
- Groups 1 and 3, which are considered in the same system, and group 2.

To compare the models, the amplification map, the convergence map and the mass of the lenses are used. The amplification map defines how much a source is magnified/demagnified based on its position in the source plane. The convergence map expresses the normalised mass distribution. Therefore, it explains the convergence of the light rays. Another name commonly used is the Kappa maps, where κ is defined as the ratio of the mean surface density and the critical density,

$$\kappa = \frac{\Sigma}{\Sigma_{cr}}. \tag{30}$$

As explained in section 3.1, when this ratio is greater than 1, the effect of the lens falls into strong gravitational lensing. The mass of the lenses is computed by summing the value of each pixel in a given region in the map of the mass distribution. This region is centred on the foreground galaxy and has a radius to cover all the observed images. All these maps are shown in Fig.17 for each model.

We observe quite different models that lead to completely different geometries of the amplification and magnification map. But it is important to note that some models did not

(a) Group 1 only.

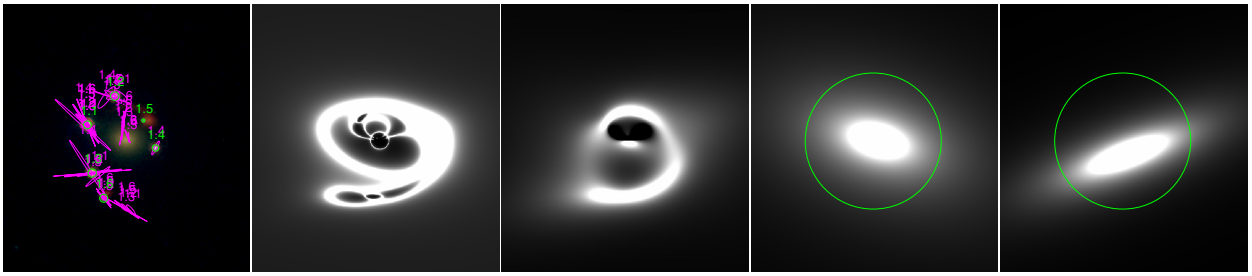

(b) Group 1 and 3 considered in the same system.

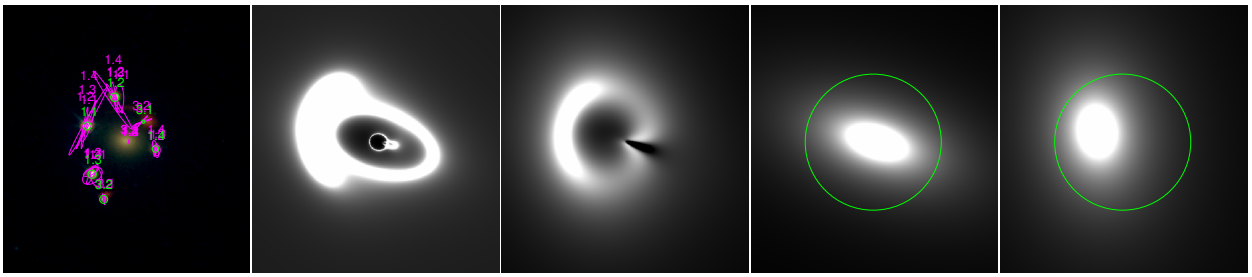

(c) Group 1 and 3 considered in a different system.

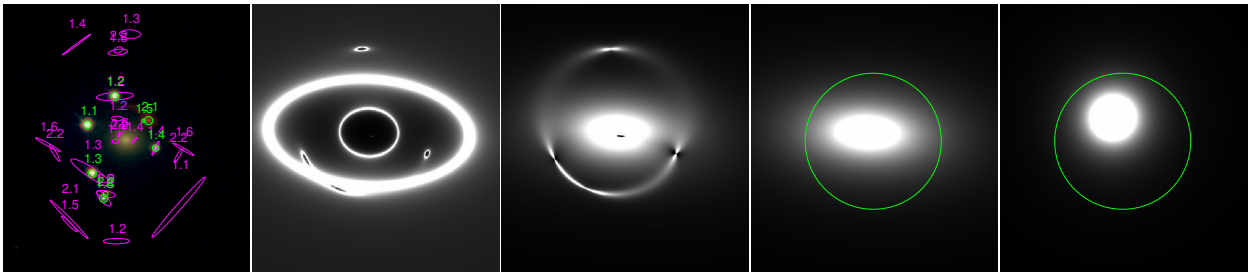

(d) Groups 1 and 3, which are considered in the same system, and group 2.

Figure 17: From left to right: Observed images and computed images; Amplification map (scaled from 0, dark, to 10, white); Convergence (Kappa) map; Mass per pixel at $z = 0.184$; Mass per pixel at $z = 1.8845$. The green region in the mass map corresponds to a disk centred at the foreground lens that includes all the images.

converge. This is clearly shown by the statistics given as output by the software. Those are listed in Table 3 with the mass of the lenses.

Group	1	1+3	1 and 3	1, 2 and 3
χ^2_{tot}	0.10	1.36	45066.15	45527.82
rms_i	0.03	0.1	0.81	1.62
log(Likelihood)	5.47	7.61	-22524.79	-22752.86
Mass L1 $[10^{12} M_\odot]$	0.5532 ± 0.06	0.5301 ± 0.05	151.4370 ± 15.1	1.0635 ± 0.11
Mass L2 $[10^{12} M_\odot]$	0.5106 ± 0.05	5.1201 ± 0.05	3.0586 ± 0.31	0.2380 ± 0.02

Table 3: Comparison of statistical tools output and total mass of the lenses between different models, considering two lens planes. Numbers in red are symptomatic of a model that did not converge. As only one test has been constructed, the error in the mass value could not be measured. We estimated the error to be 10% of the value.

The first model, presented in Fig.17a, looks like the single-plane models shown previously. This could be expected as we only input the images of the quasar created by the foreground lens. Even though those light rays have been influenced by the background galaxy, we do not provide enough constraints to the model to converge to a solution for this deflector. This is clearly shown by the rather flat parameter distribution computed thanks to the BayesCorner and shown in Fig.18. The BayesCorner is a tool that allows for visualising and computing the distribution of the posterior PDF of each parameter of the Lenstool model (developed by Mahler [29]).

The second model, presented in Fig.17b, has the same base geometry as the previous one with an extra structure present twice. This is linked to the fact that we observe two images of the background lens galaxy.
The other models did not converge, but also show the same base geometry with additional structure. In the third one, the images are well placed by the software, but it has to apply a huge penalty to obtain those results. The last one completely fails to recover the image position.

From here, we built models, fixing one of the lens models. The mass of one lens is fixed with the estimation of Dux et al. [11]. As we use the dPIE model for the mass distribution, we fixed $r_{core} = 0$ kpc[1] and $r_{cut} = 10$ kpc, leading to a value of the fiducial dispersion velocity σ_{dPIE} as

$$\sigma^2_{dPIE,km/s} = \frac{1}{2\,\pi}\frac{4}{3} M_{kg} \frac{G}{10^6\,10^3} \frac{r_{cut,km}}{r^2_{cut,km} - r^2_{core,km}}. \tag{31}$$

For $L1$ being the foreground lens and $L2$ the background one, this relation gives the values $\sigma_{dPIE,L1} = 158.156$ km/s and $\sigma_{dPIE,L2} = 145.216$ km/s.

The statistics and mass of the lens for those models are listed in Table 4.
We can note that when the foreground galaxy mass is fixed, the region covered by the

[1]The value 0.0 is not well handled by the software, the vanishing value 0.001 is applied here instead.

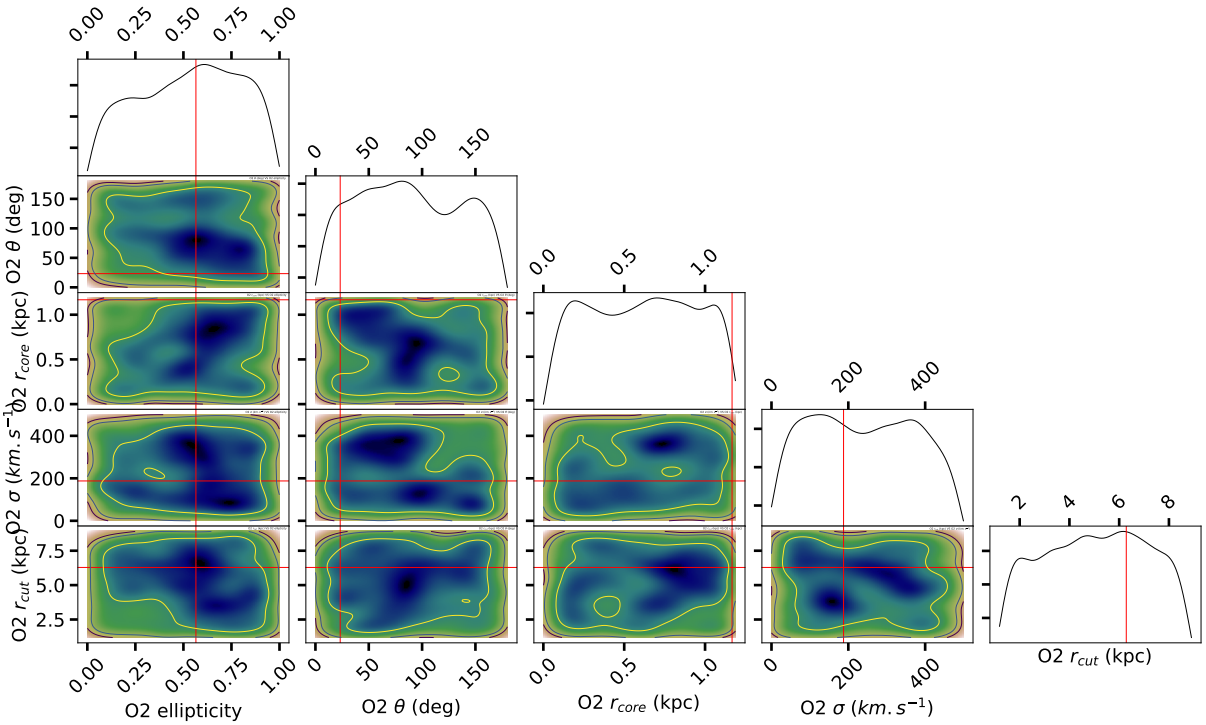

Figure 18: BayesCorner of the background lens for the multi-plane model of group 1.

amplification, and therefore, the convergence maps, is smaller. However, those models did not converge. This is either shown by the statistics, the non-recovery of the image positions by the software or a flat likelihood function of a parameter. The model, considering groups 1 and 3 in the same system, with the mass of the background lens fixed, could not recover the position of the images.

The last model did converge, and with an estimation of the mass of the first lens in the same order of magnitude as $M_1 = (2.74 \pm 0.04) \cdot 10^{11} M_\odot$, the results of Dux et al. [11].

Group	1+3, L1F	1+3, L2F	1 and 3, L1F	1 and 3, L2F
χ^2_{tot}	113268.97	45083.08	68134.99	0.6
rms_i	2.26	0.74	2.25	0.06
log(Likelihood)	-56626.2	-22533.25	-34059.21	7.99
Mass L1 $[10^{12} M_\odot]$	0.1338 ± 0.01	0.6936 ± 0.07	0.1459 ± 0.01	0.5835 ± 0.06
Mass L2 $[10^{12} M_\odot]$	0.9885 ± 0.10	0.1884 ± 0.02	1.5656 ± 0.16	0.1878 ± 0.02

Table 4: Comparison of statistical tools output and total mass of the lenses between different models, considering two lens planes with one lens mass being constrained (numbers in green). Numbers in red are symptomatic of a model that did not converge. As only one test has been constructed, the error in the mass value could not be measured. We estimated the error to be 10% of the value.

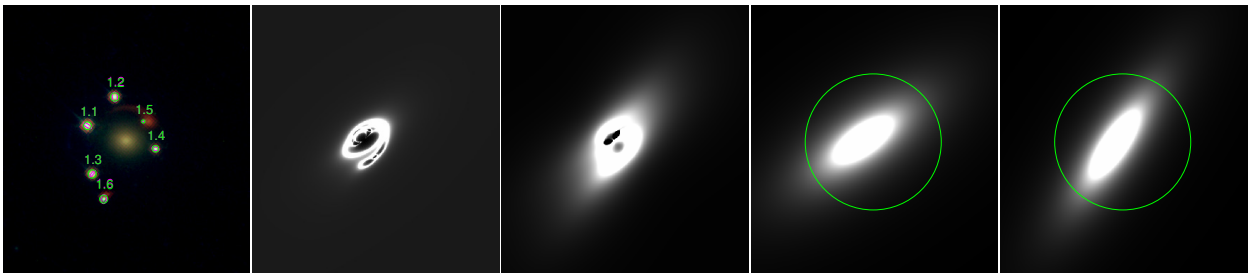

(a) Group 1 and 3 considered in the same system. The mass of the foreground lens is fixed.

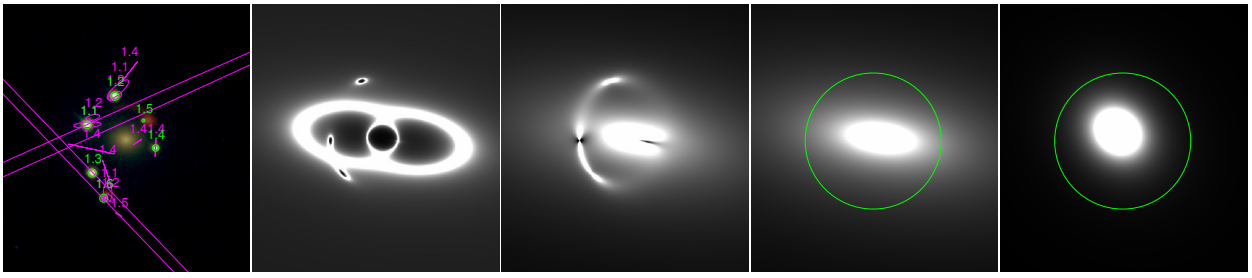

(b) Group 1 and 3 considered in the same system. The mass of the background lens is fixed.

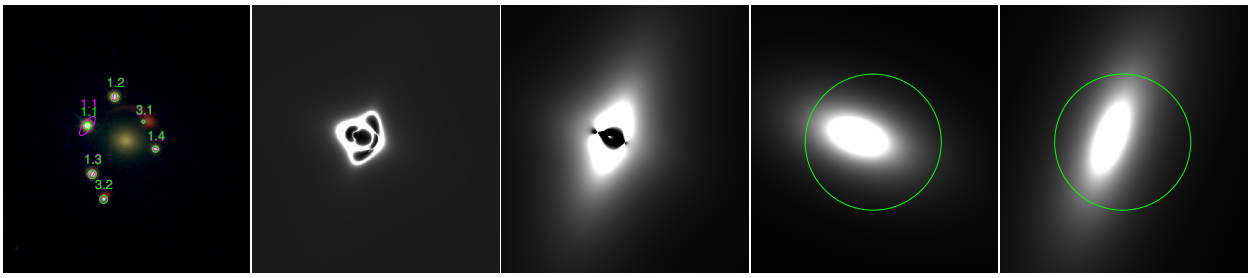

(c) Group 1 and 3 considered in a different system. The mass of the foreground lens is fixed.

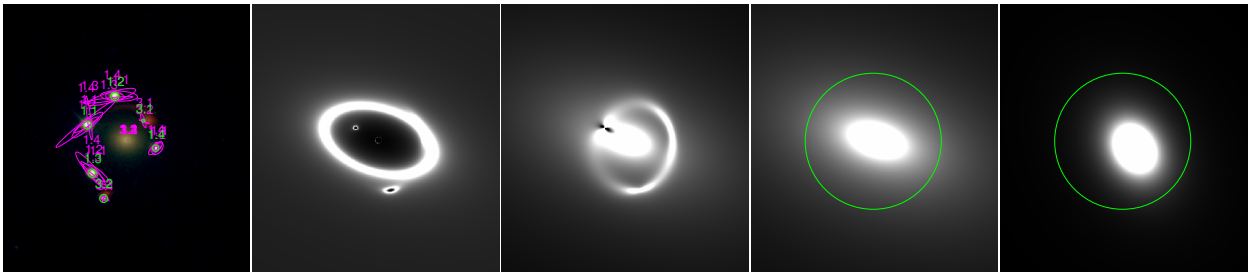

(d) Group 1 and 3 considered in a different system. The mass of the background lens is fixed.

Figure 19: From left to right: Observed images and computed images; Amplification map (scaled from 0, dark, to 10, white); Convergence (Kappa) map; Mass per pixel at $z = 0.184$; Mass per pixel at $z = 1.8845$. The green region in the mass map corresponds to a disk centred at the foreground lens that includes all the images.

With all these multi-plane models, we can note that LENSTOOL has more difficulties finding the best parameters for the background lens than for the foreground one. The full BAYESCORNER of all cases can be found in Appendix A. We also note that the software seems to better converge when groups 1 and 3 are defined as coming from the same source. It enforces LENSTOOL on the position of a single source to fit both sets of images.

5 Abell 370 overdensity between $z = 1.02$ and $z = 1.09$

The goal of this chapter is to add new mass potential along the line of sight of Abell 370 using clusters of galaxies lying between $z = 1.02$ and $z = 1.09$. The impact of the group on the position of images in the source plane is then computed.

5.1 Definition of the groups

The first step is to determine the number of groups and define them. The division into smaller groups of the overdensity between $z = 1.02$ and $z = 1.09$ has been done by Gaussian mixing. Then, we apply the Akaike Information Criterion (AIC) to find the adequate number of Gaussian curves to describe the galaxy distribution. This criterion is an estimator that balances model complexity against goodness of fit. The best require 6 groups, as shown in Fig.20.

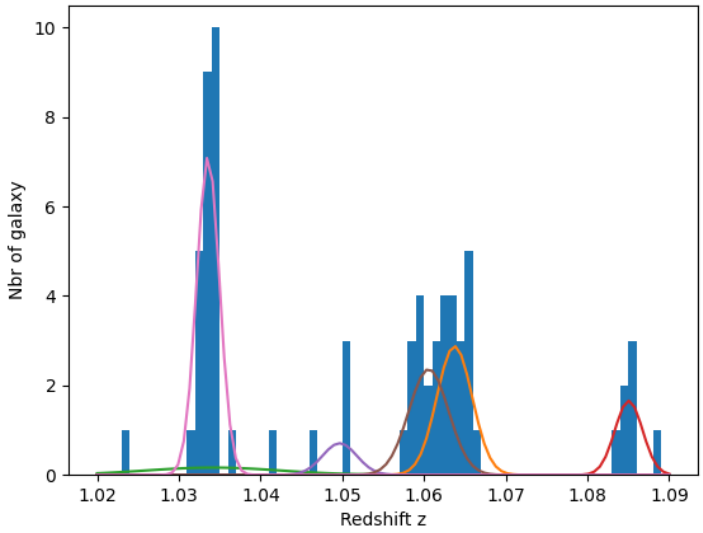

Figure 20: Best optimisation of Gaussian mixing over the overdensity between $z = 1.02$ and $z = 1.09$ of Abell 370. The number of Gaussian curves has been determined by minimisation of the AIC.

To recover the same groups as Lagattuta et al. [13], the number of groups is limited to three, and a threshold of a maximum dispersion velocity of 1500 km/s is fixed within a group. This value is a reasonable upper limit compared to typical overdensities (e.g., presented by Girardi et al. [30]). This velocity is computed with the redshift of the galaxy considered z and the mean redshift of its group from the Gaussian mixing method z_g. Using the speed of light c, this is expressed as

$$\Delta v = c \frac{|z_g - z|}{1 + \frac{z_g + z}{2}} < 1500 \text{ km/s}. \tag{32}$$

The belonging of a galaxy to a group is then refined using a sigma clipping method of $3\,\sigma$, represented by the surfaces on Fig.21.

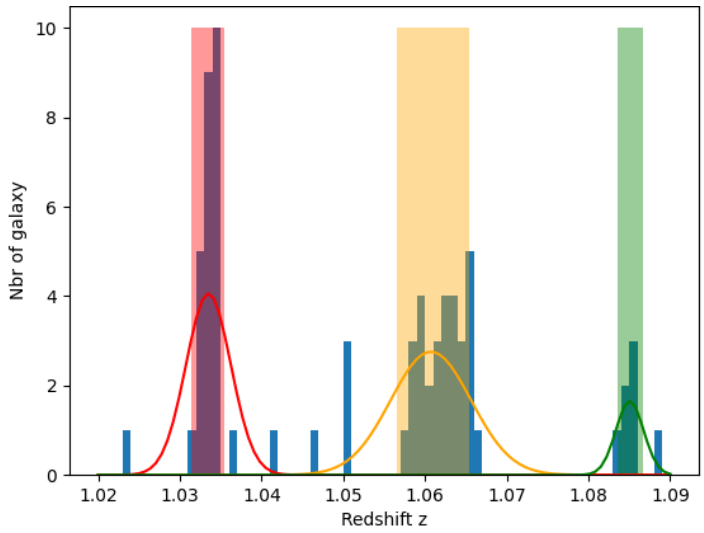

Figure 21: Gaussian mixing fixed to 3 groups and sigma clipping region, the colored boxes, used to model the overdensity between $z = 1.02$ and $z = 1.09$ of Abell 370.

The final Gaussian fit of the groups is shown in Fig.22.

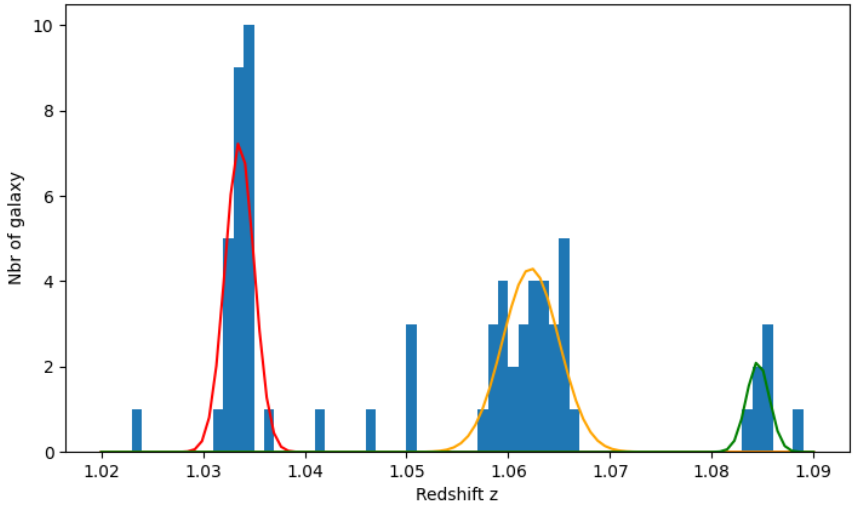

Figure 22: Gaussian fit refined by sigma clipping, which results in 3 groups to model the overdensity.

5.2 Definition of the dPIE potential

The lens potential of each group is located at the mean redshift of the final groups z_{mean}. To compute the dispersion velocity, the MAD, gapper, and biweight estimators were used,

which are shown in Table 5.

Group	z_{mean}	Nbr of galaxies	MAD	σ_{gapper} [km/s]	$\sigma_{biweight}$ [km/s]
1	1.0334	26	23.68	111.00	93.37
2	1.0610	30	21.56	229.17	233.85
3	1.0851	6	67.95	90.99	86.58

Table 5: Comparison of the different methods to estimate the velocity dispersion.

As the gapper and biweight estimators give the same order of magnitude, the value of the biweight one is arbitrarily chosen to compute M_{200} following the $\sigma - M$ relation presented by Ferragamo et al. [28] with the constant fitted on the *GIZMO-SIMBA* simulation.
The dPIE model requires as input the σ to calibrate the profile to the mass of the cluster. This value is found using the relation A25 from Elíasdóttir et al. [20] for which the core radius, r_{core}, and the cut radius, r_{cut}, are fixed respectively to zero[2] and R_{200}. All these results are shown in Table 6.

Group	$M_{200,GIZMO-SIMBA}$ $[10^{11} M_{\odot}]$	R_{200} [kpc]	σ_{dPIE} [km/s]
1	8.2957	131.225	75.96
2	109.56	306.908	180.52
3	6.8265	120.561	71.90

Table 6: M200, R200, and velocity dispersion used in the dPIE model for each group.

To place the mass potential of the 3 groups identified, we need to compute their barycenter in the source plane. The position of the galaxies of each group in the source plane is retrieved thanks to the software LENSTOOL using the model of Niemiec et al. [25]. The barycenter position tends toward more massive galaxies. This has been implemented by combining the velocity dispersion and a coefficient related to the magnitude of the galaxy in the F160W filter. This last one is computed as follows

$$c_{galaxy} = \begin{cases} 1 & \text{if } F160W_{galaxy} = 99.99 \text{ (i.e., unknown)}, \\ 10 - 8\left(\frac{F160W_{galaxy} - min(F160W_{group})}{max(F160W_{group}) - min(F160W_{group})}\right) & \text{otherwise} \end{cases} \tag{33}$$

resulting in a linear scale between 1 and 10, giving more weight to the brighter galaxy, i.e., the more massive one. The computed barycentres are shown in Table 7.

Group	z_{mean}	RA [deg]	DEC [deg]
1	1.0334	39.96715734741958	-1.5717530298410765
2	1.0610	39.96585655466668	-1.5841142669820423
3	1.0851	39.96863954669002	-1.5711790188899013

Table 7: Redshift and barycentre position of each group.

[2]The value 0.0 is not well handled by the software, the vanishing value 0.00001 is applied here instead.

Assuming a spherical potential, we now have all the information needed to add the potential generated by each group in the LENSTOOL model.

5.3 Impact of the background groups on the model

To measure the impact of those potentials, we use a set of gold-tier background galaxies from the model of Niemiec et al. [25], from which we have removed all the images coming from sources standing in front of at least one potential, as this case is not supported by the LENSTOOL software. We place the farthest potential at redshift $z = 1.0851$. Therefore, all sources placed at an inferior redshift are deleted. As we do not want to optimise the model, this would not impact the result of the other sources. However, considering them might be non-negligible for optimising the lens model.
As expected, the addition of those has slightly shifted the position of the source. This difference can be computed and is shown in the diagram of Fig.23.

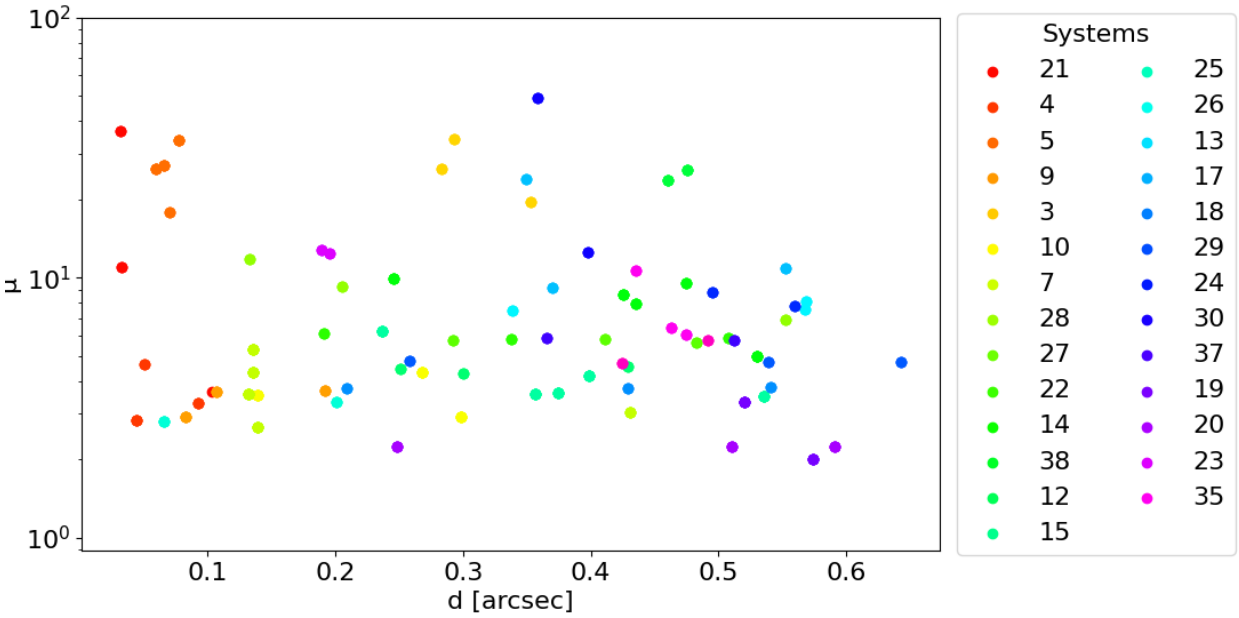

Figure 23: Diagram of the magnification against the distance of the source between the model with and without the group potential added to the model. Each color represents a different system, and each point is linked to an image in the source plane.

It shows that there is no significant trend between the difference in the position and the amplification. But also that the difference in the distance is non-negligible. The best lens model *rms* can be as low as 0.2 arcseconds, while others can have values as high as 1.0 arcseconds (e.g., the model presented by Cerny et al. [31]). For the best models, taking into account the potentials along the line of sight has a significant impact on the model.

6 Conclusion and prospectives

In this work, we compared single-plane strong gravitational lensing with multi-plane strong lensing to understand the influence of an additional mass potential along the line of sight. This has been realised using various configurations of galaxies and clusters of galaxies. Consider the multi-plane aspect of these rare cases of lenses, which gives a more accurate estimation of the lens properties, such as the mass distribution.

We focus first on a Galaxy-Galaxy case thanks to the Zig-Zag lens. Three image groups were defined based on the source and path of the light rays. We build different models based on various associations of the image groups in the single-plane approximation of the lens geometry. We observe that the lens geometry was conserved, whereas other groups of images were used. These models give an estimation of the mass of the foreground lens equal to $M_1 \approx 6 \cdot 10^{11} M_\odot$, whereas the value obtained by Dux et al. [11] equals $M_1 = (2.74 \pm 0.04) \cdot 10^{11} M_\odot$. Then, we introduce the double-plane aspect of the lens and vary the associations of groups, comparing them. They result in different geometries of lenses but conserve a quite similar base close to the single-plane models for the foreground lens. However, some models did not converge. The posterior parameter distributions of the background lens are rather flat, as indicated by the BayesCorner tool. To overcome this problem, the total mass of one of the lenses is fixed using the result of Dux et al. [11]: $M_1 = (2.74 \pm 0.04) \cdot 10^{11} M_\odot$ and $M_2 = (2.31 \pm 0.19) \cdot 10^{11} M_\odot$. Then, we ask the software to optimise the parameters of the other one. Only one of these models converged, giving a total mass estimation for the foreground lens slightly smaller than the single-plane models, $M_1 = (5.835 \pm 0.58) \cdot 10^{11} M_\odot$, which is of the same order as Dux et al. [11].
Several solutions might alleviate our reported issues. The rather strong external shear reported by Dux et al. [11] and in this work remains degenerated with other parameters in our model. Decreasing the number of parameters for the potentials might be interesting, as we did by fixing the mass of the lenses. Other methods, such as dynamical mass estimates, can be used to fulfil this objective. We expect to observe a decrease in the mass attributed to the external shear as the multi-plane configuration of the lens has been considered and not approximated by a single plane.

The second focus on the Cluster-Cluster case was based on the overdensity of galaxies between $z = 1.02$ and $z = 1.09$ of Abell 370. An analysis of the redshift distribution reveals 3 overdensities of galaxies. These groups are respectively located at $z_{mean,1} = 1.0334$, $z_{mean,2} = 1.0610$, and $z_{mean,3} = 1.0851$. We computed the mass of these potentials based on their dispersion velocity using one of the $\sigma - M$ relations, which accounts for the redshift of the object, proposed by Ferragamo et al. [28]. The velocity dispersion σ was computed based on the redshift of the galaxies using the biweight estimator. The masses obtained for the 3 groups are $M_{200,1} = 8.2957 \cdot 10^{11} M_\odot$, $M_{200,2} = 109.56 \cdot 10^{11} M_\odot$, and $M_{200,3} = 6.8265 \cdot 10^{11} M_\odot$. To place these potentials spatially, we used the model of Niemiec et al. [25] to compute the position in the source plane of each galaxy. With this information, we computed the barycen-

tre weighted by the luminosity of the galaxies (i.e., their mass, as mass and luminosity are proportional). We compare the position of the images projected onto the source plane and measure a non-negligible impact of structures along the line of sight. The difference in position of the image in the source plane could be as high as 0.6 arcseconds, where the current best lens models show a typical root-mean-squared for position uncertainty ranging from 0.2 to 1.0 arcseconds.
To improve the accuracy of the Abell 370 model, it would be interesting to investigate a subdivision of the group at redshift $z = 1.0610$. However, the number of galaxies in this group is rather small, which might lead to a negligible effect. Moreover, in this work, we modify a model of Abell 370 by adding mass potential along the line of sight. A more accurate model of Abell 370 requires the optimisation of the lens model with these potentials. We expect to decrease the amplitude of the external shear field, often associated with unaccounted mass or a change in mass distribution, as it would not compensate for the effect of the potentials behind the cluster. In addition, we deleted the multiple images lying between the new potential and the foreground lens, as their position made them impossible to handle by the LENSTOOL software. This represents 7 systems over 33 multiple-image systems.

A following work aiming to cover the Cluster-Galaxy case should use the observation of a galaxy identified by Mahler et al. [19] as being behind Abell 2744. Another case that could be covered is the Galaxy-Cluster one. For this, the example of MACSJ0416 can be utilised (e.g., Jauzac et al. [32]).

We conclude that structure along the line-of-sight can have a significant impact on the lensing geometry, and this at multiple scales. This impact offers peculiar configurations, such as the Zig-Zag lens. The mass distribution of the foreground structure is also significantly affected, generating a displacement challenging the current accuracy of the lens models.

Appendix A BayesCorner

A.1 Group 1 only

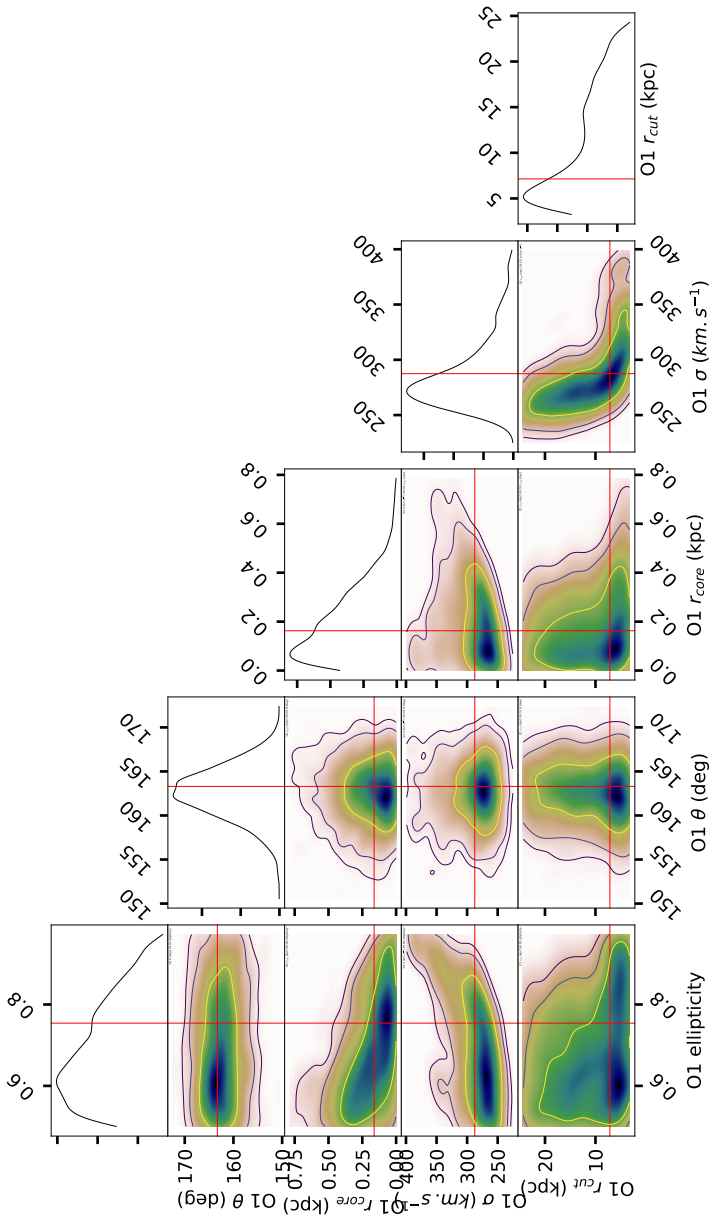

Figure 24: BayesCorner of the foreground lens for the multi-plane model of group 1. We observe a good convergence of the parameters of the foreground lens.

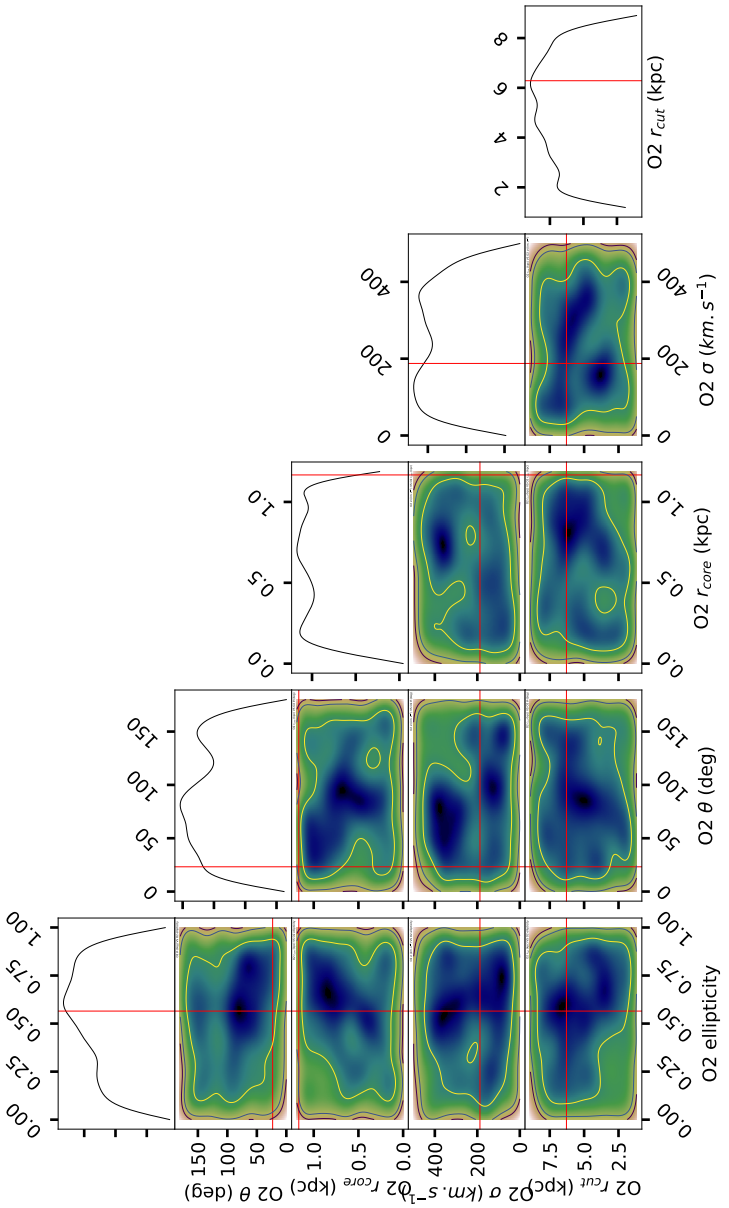

Figure 25: BayesCorner of the background lens for the multi-plane model of group 1. We observe no convergence of the parameters of the background lens.

A.2 Groups 1 and 3 considered as one group

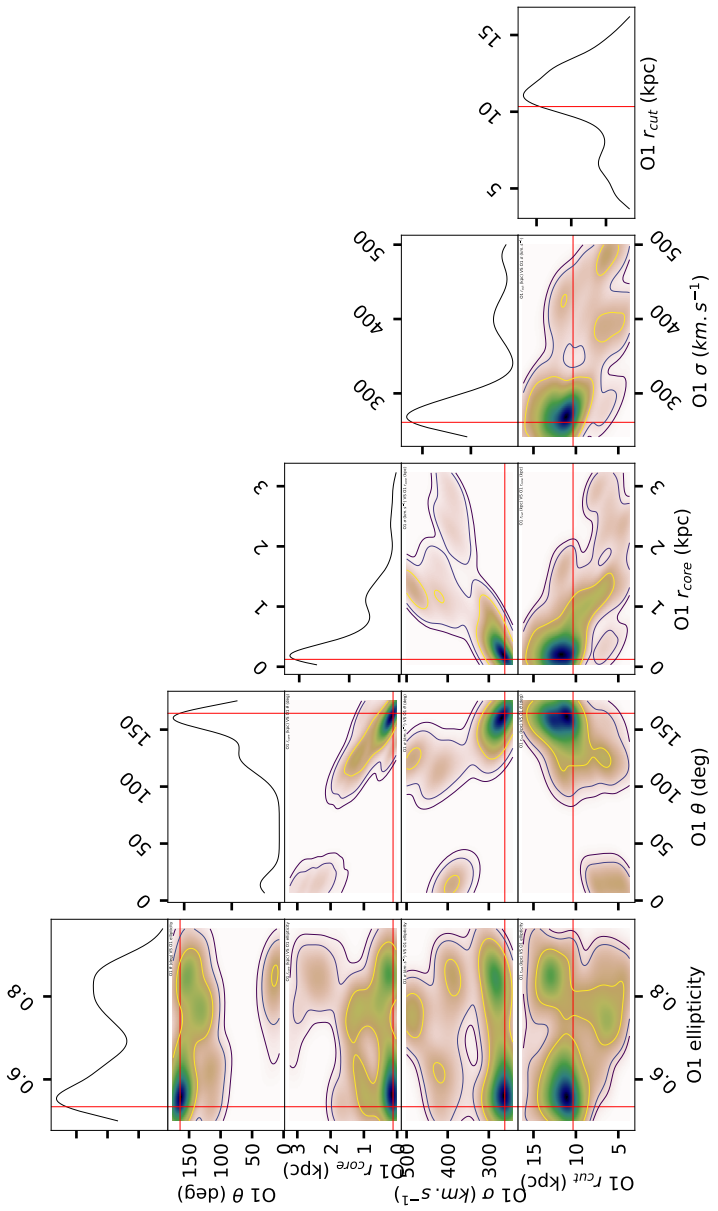

Figure 26: BayesCorner of the foreground lens for the multi-plane model of groups 1 and 3 considered as one group. We observe a good convergence of the parameters of the foreground lens.

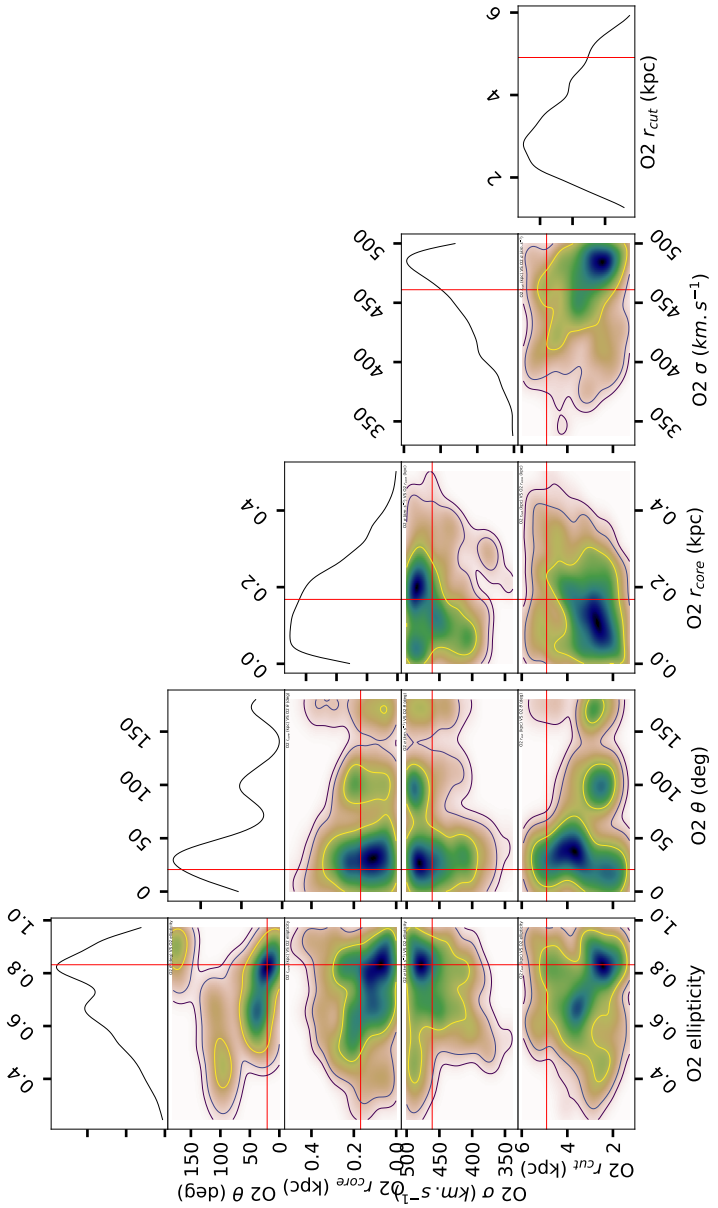

Figure 27: BayesCorner of the background lens for the multi-plane model of groups 1 and 3 considered as one group. We observe quite a good convergence of the parameters of the background lens.

A.3 Groups 1 and 3 considered as different groups

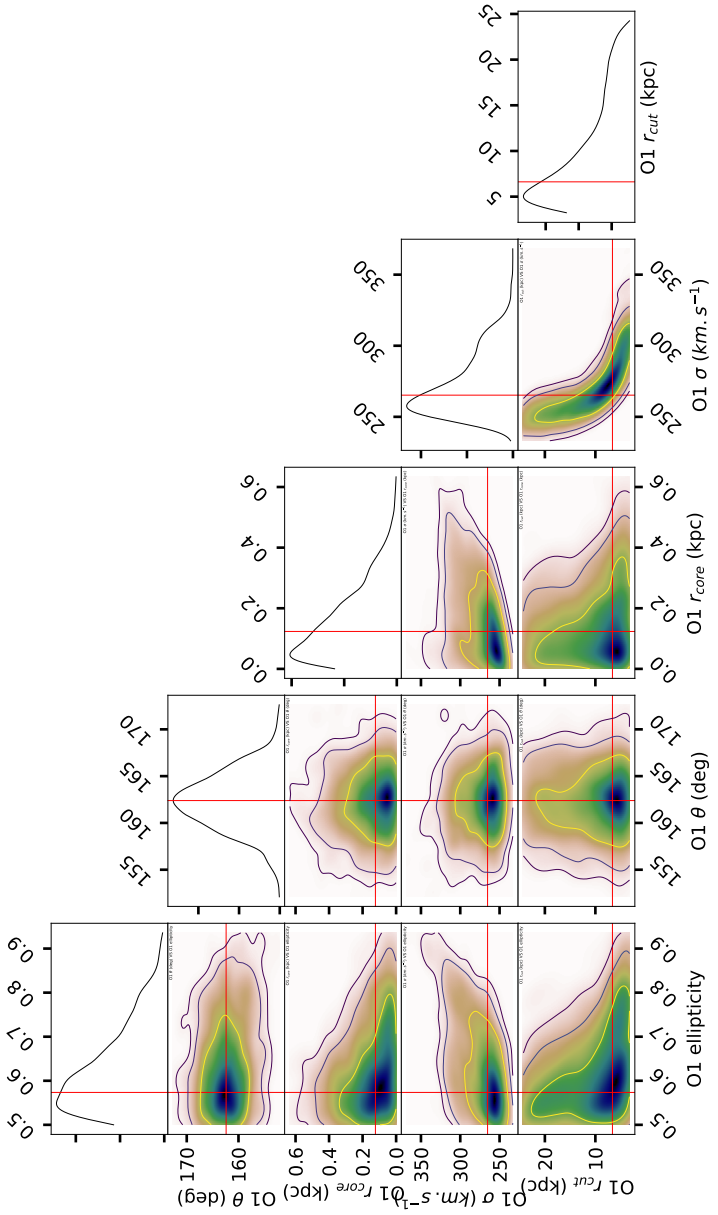

Figure 28: BayesCorner of the foreground lens for the multi-plane model of groups 1 and 3 considered as different groups. We observe a good convergence of the parameters of the foreground lens.

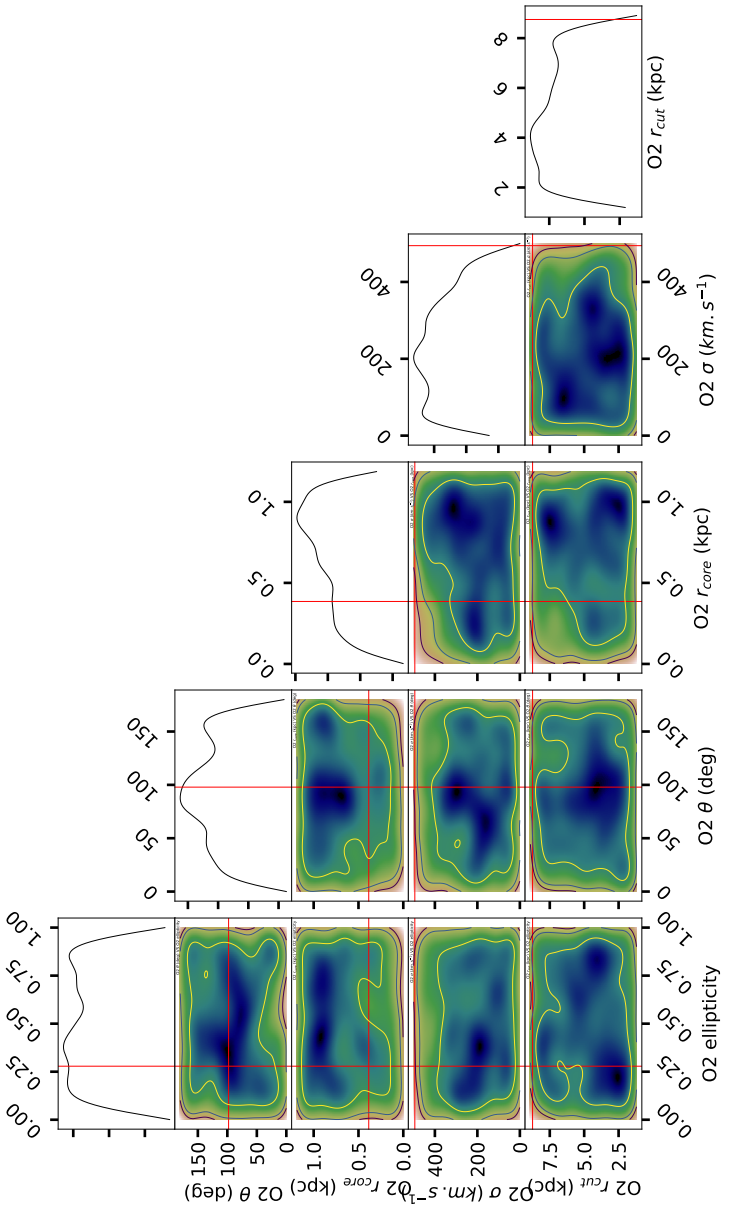

Figure 29: BayesCorner of the background lens for the multi-plane model of groups 1 and 3 considered as different groups. We observe no convergence of the parameters of the background lens.

A.4 Groups 1 and 3 considered as one group with group 2

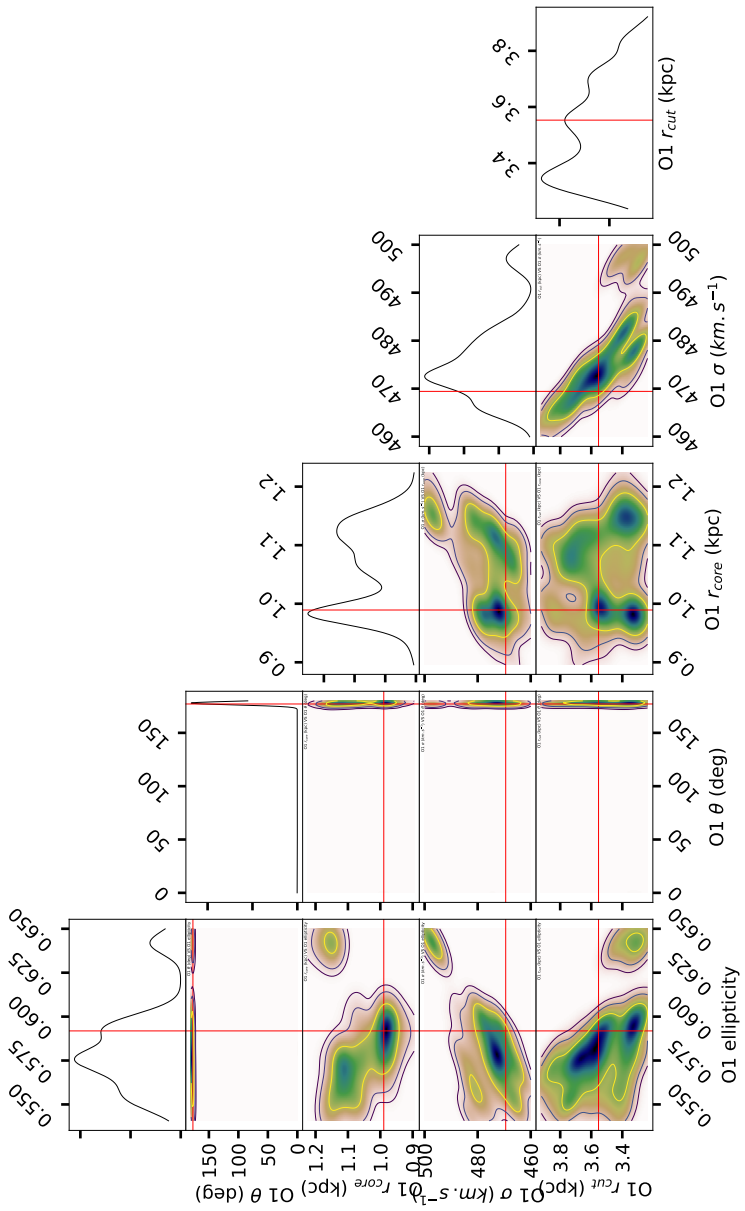

Figure 30: BayesCorner of the foreground lens for the multi-plane model of groups 1 and 3 considered as one group with group 2. We observe a good convergence of the parameters of the foreground lens.

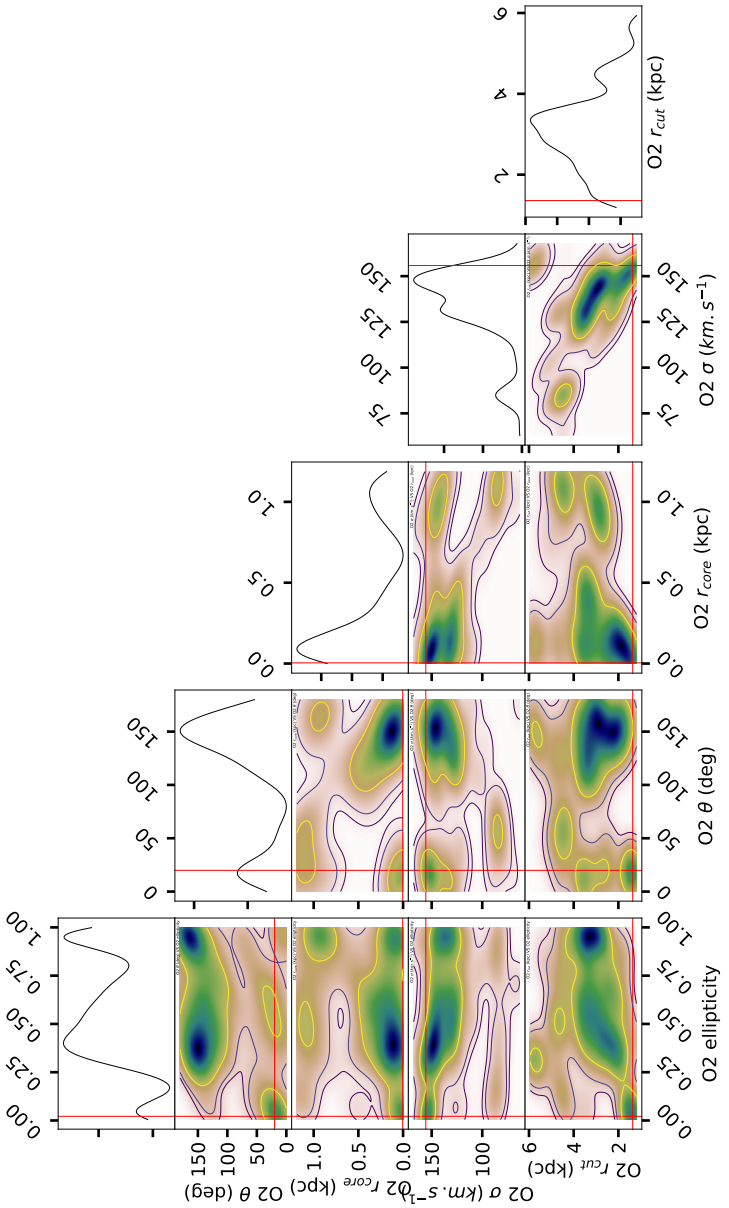

Figure 31: BayesCorner of the background lens for the multi-plane model of groups 1 and 3 considered as one group with group 2. We observe quite a good convergence of the parameters of the background lens.

A.5 Groups 1 and 3 considered as one group with the mass of the foreground lens fixed

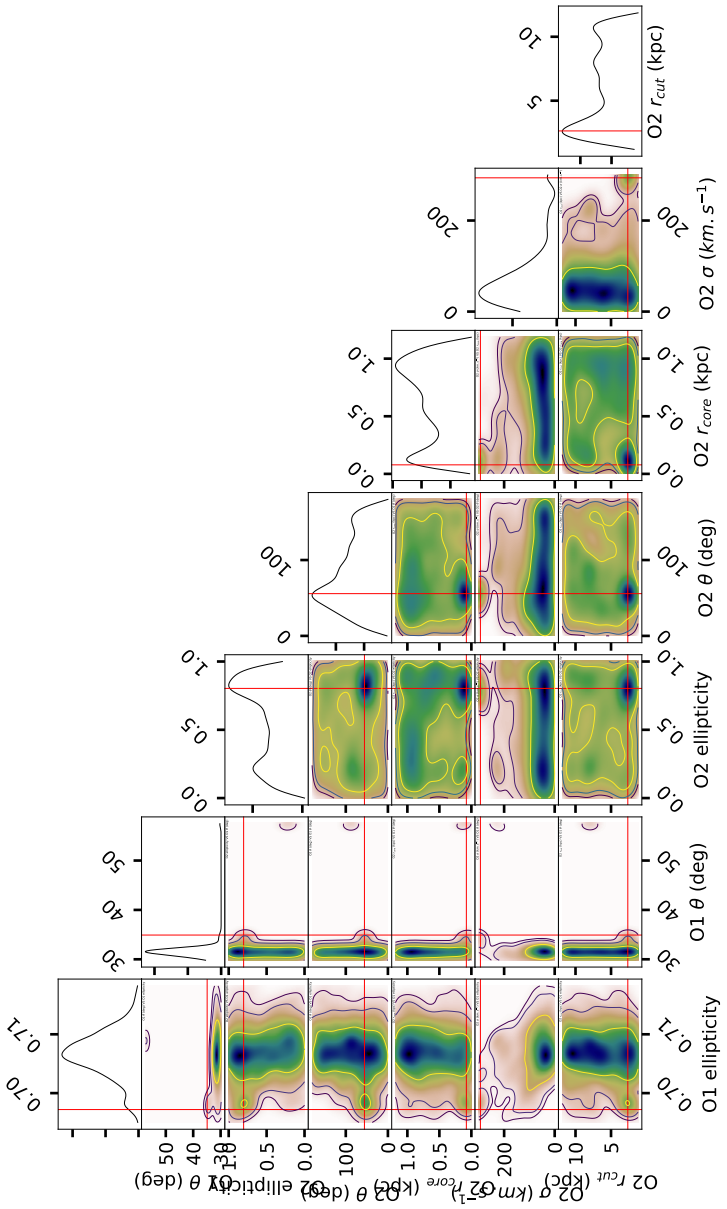

Figure 32: BayesCorner of the background lens for the multi-plane model of groups 1 and 3 considered as one group with the mass of the foreground lens fixed. We observe a good convergence of the free parameters of the foreground lens, but no convergence for the background one.

A.6 Groups 1 and 3 considered as one group with the mass of the background lens fixed

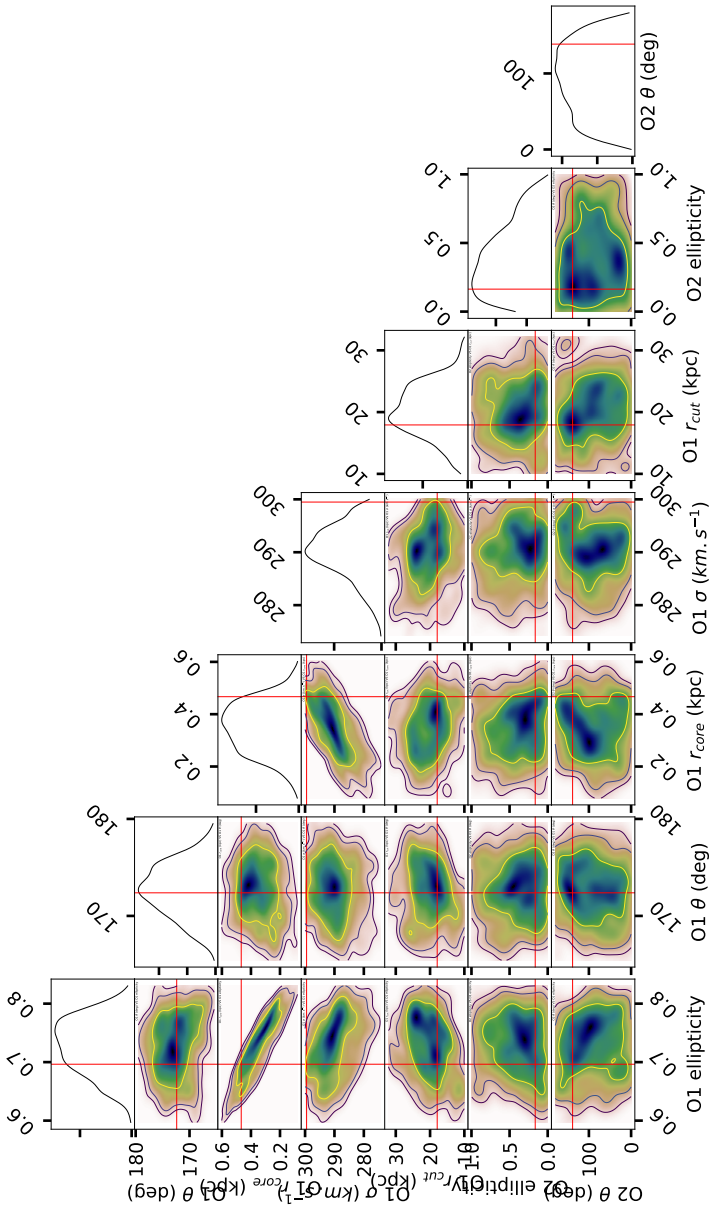

Figure 33: BayesCorner of the foreground lens for the multi-plane model of groups 1 and 3 considered as one group with the mass of the background lens fixed. We observe quite a good convergence of the parameters of the foreground lens and the free parameters of the background one.

A.7 Groups 1 and 3 considered as different groups with the mass of the foreground lens fixed

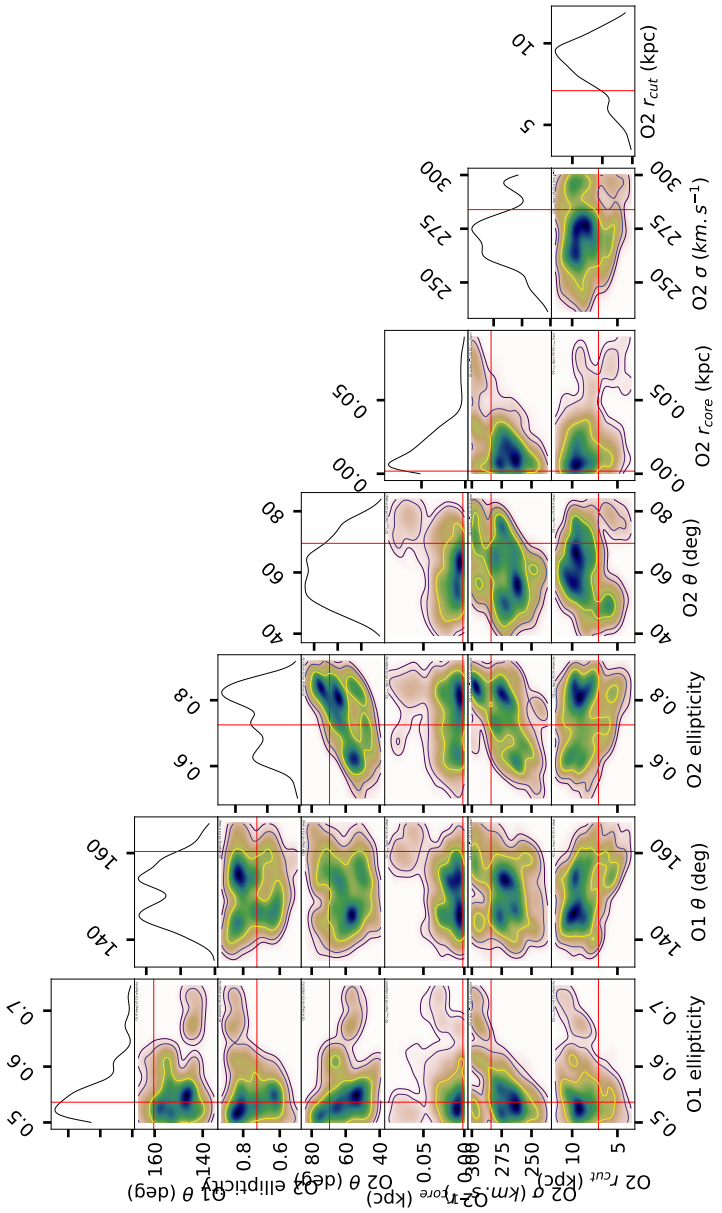

Figure 34: BayesCorner of the background lens for the multi-plane model of groups 1 and 3 considered as different groups with the mass of the foreground lens fixed. We observe quite a good convergence of the parameters of the lenses.

A.8 Groups 1 and 3 considered as different groups with the mass of the background lens fixed

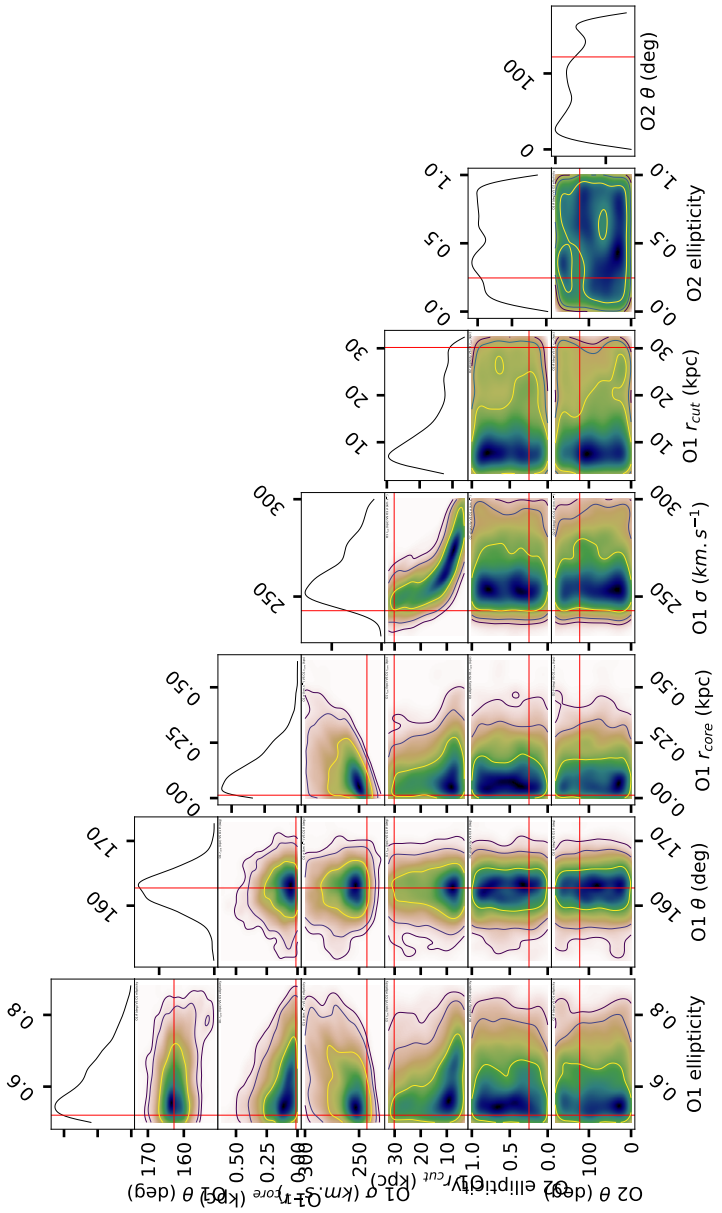

Figure 35: BayesCorner of the foreground lens for the multi-plane model of groups 1 and 3 considered as different groups with the mass of the background lens fixed. We observe quite a good convergence of the parameters of the foreground lens, but no convergence for the background one.

Bibliography

[1] Joachim Wambsganss. "Gravitational Lensing in Astronomy". In: *Living Reviews in Relativity* 1.2 (Dec. 1998). ISSN: 1433-8351. DOI: 10.12942/lrr-1998-12. URL: https://doi.org/10.12942/lrr-1998-12.

[2] Peter Coles. "A revolution in science: the eclipse expeditions of 1919". In: *Contemporary Physics* 60.1 (Jan. 2019), pp. 45–59. ISSN: 1366-5812. DOI: 10.1080/00107514.2019.1624000. URL: http://dx.doi.org/10.1080/00107514.2019.1624000.

[3] Keel Bildad. *The double QSO 0957+561*. Consulted the 29th June 2025. URL: https://pages.astronomy.ua.edu/keel/agn/q0957.html.

[4] G. Soucail et al. "The giant arc in A 370 : spectroscopic evidence for gravitational lensing from a source at Z=0.724." In: *Astronomy & Astrophysics* 191 (Feb. 1988), pp. L19–L21.

[5] Matthew B. Bayliss et al. "Line-of-sight Structure toward Strong Lensing Galaxy Clusters". In: *The Astrophysical Journal* 783.1, 41 (Mar. 2014), p. 41. DOI: 10.1088/0004-637X/783/1/41. arXiv: 1312.3637 [astro-ph.CO].

[6] Joachim Wambsganss, Paul Bode, and Jeremiah P. Ostriker. "Gravitational Lensing in a Concordance ΛCDM Universe: The Importance of Secondary Matter along the Line of Sight". In: *The Astrophysical Journal* 635.1 (Nov. 2005), p. L1. DOI: 10.1086/498976. URL: https://dx.doi.org/10.1086/498976.

[7] Ewald Puchwein and Stefan Hilbert. "Cluster strong lensing in the Millennium simulation: the effect of galaxies and structures along the line-of-sight". In: *Monthly Notices of the Royal Astronomical Society* 398.3 (Sept. 2009), pp. 1298–1308. ISSN: 0035-8711. DOI: 10.1111/j.1365-2966.2009.15227.x. eprint: https://academic.oup.com/mnras/article-pdf/398/3/1298/4090216/mnras0398-1298.pdf. URL: https://doi.org/10.1111/j.1365-2966.2009.15227.x.

[8] Christopher S. Kochanek and John Apostolakis. "The two-screen gravitational lens". In: *Monthly Notices of the Royal Astronomical Society* 235.4 (Dec. 1988), pp. 1073–1109. ISSN: 0035-8711. DOI: 10.1093/mnras/235.4.1073. eprint: https://academic.oup.com/mnras/article-pdf/235/4/1073/2965138/mnras235-1073.pdf. URL: https://doi.org/10.1093/mnras/235.4.1073.

[9] Thomas E. Collett and David J. Bacon. "Compound lensing: Einstein zig-zags and high-multiplicity lensed images". In: *Monthly Notices of the Royal Astronomical Society* 456.2 (Dec. 2015), pp. 2210–2220. ISSN: 1365-2966. DOI: 10.1093/mnras/stv2791. URL: http://dx.doi.org/10.1093/mnras/stv2791.

[10] Ole Möller and A.W. Blain. "Strong gravitational lensing by multiple galaxies". In: *Monthly Notices of the Royal Astronomical Society* 327.1 (Oct. 2001), pp. 339–349. ISSN: 0035-8711. DOI: 10.1046/j.1365-8711.2001.04727.x. eprint: https://academic.oup.com/mnras/article-pdf/327/1/339/4115290/327-1-339.pdf. URL: https://doi.org/10.1046/j.1365-8711.2001.04727.x.

[11] F. Dux et al. *J1721+8842: The first Einstein zig-zag lens*. 2024. arXiv: 2411.04177 [astro-ph.CO]. URL: https://arxiv.org/abs/2411.04177.

[12] C. Lemon et al. "J1721+8842: a gravitationally lensed binary quasar with a proximate damped Lyman-α absorber". In: *Astronomy & Astrophysics* 657 (Jan. 2022), A113. ISSN: 1432-0746. DOI: 10.1051/0004-6361/202142138. URL: http://dx.doi.org/10.1051/0004-6361/202142138.

[13] David J Lagattuta et al. "Pilot-WINGS: An extended MUSE view of the structure of Abell 370". In: *Monthly Notices of the Royal Astronomical Society* 514.1 (June 2022), pp. 497–517. ISSN: 0035-8711. DOI: 10.1093/mnras/stac418. eprint: https://academic.oup.com/mnras/article-pdf/514/1/497/50484627/stac418.pdf. URL: https://doi.org/10.1093/mnras/stac418.

[14] N. Straumann. "Weak and Strong Lensing Statistics". In: *Space Science Reviews* 100.1/4 (2002), pp. 29–38. ISSN: 0038-6308. DOI: 10.1023/a:1015801707999. URL: http://dx.doi.org/10.1023/A:1015801707999.

[15] Peter Schneider, Jürgen Ehlers, and Emilio E. Falco. *Gravitational Lenses*. Springer Berlin, Heidelberg, 1992. DOI: https://doi.org/10.1007/978-3-662-03758-4.

[16] Matthew B. Bayliss, Keren Sharon, and Traci Johnson. "Quantifying the Impact of Cosmological Parameter Uncertainties on Strong-lensing Models with an Eye Toward the Frontier Fields". In: *The Astrophysical Journal* 802.1, L9 (Mar. 2015), p. L9. DOI: 10.1088/2041-8205/802/1/L9. arXiv: 1412.6807 [astro-ph.CO].

[17] Eric Jullo et al. "A Bayesian approach to strong lensing modelling of galaxy clusters". In: *New Journal of Physics* 9.12 (2007), p. 447.

[18] Keren Sharon et al. "RELICS: A Strong-lens Model of SMACS J0723.3-7327". In: *The Astrophysical Journal* 264.1, 15 (Jan. 2023), p. 15. DOI: 10.3847/1538-4365/aca7c3. arXiv: 2208.08483 [astro-ph.GA].

[19] G. Mahler et al. "Strong-lensing analysis of A2744 with MUSE and Hubble Frontier Fields images". In: *Monthly Notices of the Royal Astronomical Society* 473.1 (Aug. 2017), pp. 663–692. ISSN: 1365-2966. DOI: 10.1093/mnras/stx1971. URL: http://dx.doi.org/10.1093/mnras/stx1971.

[20] Árdís Elíasdóttir et al. *Where is the matter in the Merging Cluster Abell 2218?* 2007. arXiv: 0710.5636 [astro-ph]. URL: https://arxiv.org/abs/0710.5636.

[21] Marceau Limousin. *Contraintes sur la Distribution de Masse des Galaxies par Cisaillement Gravitationnel*. Soutenance de thèse, Laboratoire d'Astrophysique de l'Observatoire Midi-Pyrénées. June 2004.

[22] Peter Schneider. "Generalized multi-plane gravitational lensing: time delays, recursive lens equation, and the mass-sheet transformation". In: *Astronomy & Astrophysics* 624 (2019), A54.

[23] Cameron A Lemon et al. "Gravitationally lensed quasars in Gaia–II. Discovery of 24 lensed quasars". In: *Monthly Notices of the Royal Astronomical Society* 479.4 (2018), pp. 5060–5074.

[24] J. M. Lotz et al. "The Frontier Fields: Survey Design and Initial Results". In: *The Astrophysical Journal* 837.1 (Mar. 2017), p. 97. DOI: 10.3847/1538-4357/837/1/97. URL: https://dx.doi.org/10.3847/1538-4357/837/1/97.

[25] A. Niemiec et al. "Beyond the ultradeep frontier fields and legacy observations (BUFFALO): a high-resolution strong+weak-lensing view of Abell 370". In: *MNRAS* 524.2 (Sept. 2023), pp. 2883–2910. DOI: 10.1093/mnras/stad1999. arXiv: 2307.03778 [astro-ph.CO].

[26] David J Lagattuta et al. "Probing 3D Structure with a Large MUSE Mosaic: Extending the Mass Model of Frontier Field Abell 370". In: *Monthly Notices of the Royal Astronomical Society* (Mar. 2019). ISSN: 1365-2966. DOI: 10.1093/mnras/stz620. URL: http://dx.doi.org/10.1093/mnras/stz620.

[27] Timothy C Beers, Kevin Flynn, and Karl Gebhardt. "Measures of location and scale for velocities in clusters of galaxies-A robust approach". In: *Astronomical Journal (ISSN 0004-6256), vol. 100, July 1990, p. 32-46.* 100 (1990), pp. 32–46.

[28] Ferragamo, Antonio et al. "Velocity dispersion vs cluster mass: A new scaling law with The Three Hundred clusters". In: *EPJ Web Conf.* 257 (2022), p. 00018. DOI: 10.1051/epjconf/202225700018. URL: https://doi.org/10.1051/epjconf/202225700018.

[29] Guillaume Mahler. "Modélisation précise d'amas de galaxies massifs observés par Hubble et MUSE". PhD thesis. Université de Lyon, 2017.

[30] Marisa Girardi et al. "Velocity dispersions and X-ray temperatures of galaxy clusters". In: *arXiv preprint astro-ph/9507031* (1995).

[31] Catherine Cerny et al. "Strong LensIng and Cluster Evolution (SLICE) with JWST: Early Results, Lens Models, and High-Redshift Detections". In: *arXiv e-prints*, arXiv:2503.17498 (Mar. 2025), arXiv:2503.17498. DOI: 10.48550/arXiv.2503.17498. arXiv: 2503.17498 [astro-ph.CO].

[32] M. Jauzac et al. "Hubble Frontier Fields: a high-precision strong-lensing analysis of galaxy cluster MACSJ0416.1-2403 using ∼200 multiple images". In: *MNRAS* 443.2 (Sept. 2014), pp. 1549–1554. DOI: 10.1093/mnras/stu1355. arXiv: 1405.3582 [astro-ph.CO].

[33] SJUR REFSDAL. "DETERMINATION OF H_0 AND THE MASS DISTRIBUTION IN THE LENSING GALAXY FROM THE TIME DELAY EFFECT". In: *Thinking, Observing and Mining the Universe*. 2004, pp. 231–235. DOI: 10.1142/9789812702999_0027. eprint: https://www.worldscientific.com/doi/pdf/10.1142/9789812702999_0027. URL: https://www.worldscientific.com/doi/abs/10.1142/9789812702999_0027.

[34] S. Refsdal and Jean Surdej. “Gravitational lenses”. English. In: *Reports on Progress in Physics* 57 (1994). ISSN: 0034-4885. DOI: 10.1088/0034-4885/57/2/001. URL: http://esoads.eso.org/abs/1994RPPh...57..117R.